Analytical Modelling and Optimization of Output Voltage Harmonic Spectra of Full-Bridge Modular Multilevel Converters in Boost Mode

Sumeet Singh Thakur, Milijana Odavic, *Member, IEEE*, Ahmed Allu, Z. Q. Zhu, *Fellow, IEEE*, and Kais Atallah

***Abstract*—This article develops a new closed-form analytical solution to the harmonic spectrum of the full-bridge (FB) modular multilevel converter (MMC) with phase shifted carrier pulse width modulation. It considers FB-MMC operation in boost mode where the negative-voltage states of the FB submodules (SMs) are utilized to extend the ac operating voltage range and/or reduce the dc link voltage which is known to reduce the energy storage requirement. The solution is based on double Fourier series expansion in two variables. The harmonic distribution of the output voltage is analyzed and the effects of the modulation index and the number of SMs on the output voltage harmonics are revealed. The influence of the upper/lower arm carrier phase shift angle is also investigated. Using the analysis, selection of the number of SMs, the modulation index and the upper/lower arm carrier phase shift angle are specified for output voltage harmonic minimization. The findings are verified by simulation and experimental results.**

***Index Terms*—Analytical modelling, full bridge (FB) submodule (SM), harmonic spectrum, modular multilevel converter (MMC), negative-voltage states.**

NOMENCLATURE

$x = \{a, b, c\}$	Phase *a, b, c*.
$r = \{u, l\}$	Upper arm, lower arm.
$k = \{1, 2, 3 \ldots N\}$	kth SM in an arm.
N	Number of cascaded SMs in one arm.
M_0	DC component in the modulation signal.
M_1	Amplitude of modulation signal fundamental component.
$M_x^{r,k}$	Modulation signal of upper/lower arm kth SM.
$M_{x,LL}^{r,k}$	Modulation signal of upper/lower arm kth SM left leg.
$M_{x,RL}^{r,k}$	Modulation signal of upper/lower arm kth SM right leg.
ω_o	Grid frequency (rad/s). $\omega_o = 2\pi f_o$.
θ_x	Initial phase shift of the phase x ($\theta_x = \{0, -2\pi/3, 2\pi/3\}$ for $x = \{a, b, c\}$).
v_{gx}	AC side/grid side phase voltage (V).
v_{mx}	MMC fundamental phase voltage (V).
v_{ox}	MMC PWM phase voltage (V).
i_x	AC side/grid side phase current (A).
V_g	Amplitude of ac side/grid side phase voltage (V).
V_m	Amplitude of MMC phase voltage (V).
I_m	Amplitude of ac side/grid side phase current (A).
ϕ_m	AC current phase angle (rad).
E	DC side voltage (V).
k_m	Converter modulation index (ac to dc voltage ratio).
i_{dc}	DC side current (I_{dc} in steady-state) (A).
$v_{x,LN}^{r,k}$	Left leg output voltage of kth SM in upper/lower arm (V).
$v_{x,RN}^{r,k}$	Right leg output voltage of kth SM in upper/lower arm (V).
$v_x^{r,k}$	AC/output side voltage of kth SM in upper/lower arm (V).
v_x^r	Upper/lower arm voltage of phase x (V).
$v_{c,x}^{r,k}$	SM capacitor voltage of kth SM in upper/lower arm (V).
V_c^0	DC/average value of SM capacitor voltages (V).
ΔV_c	SM capacitor voltage ripple (%).
e_x^r	Instantaneous arm energy variation (J).
Δe	Arm energy peak-peak ripple (J).
i_x^r	Upper/lower arm current of phase x (A).
$i_{z,x}$	Circulating current of phase x (A).
R_b	Effective arm resistance (Ω).
L_b	Inductance of arm inductor *(H)*.
R_g	Resistance of ac/grid side filter/transformer (Ω).
L_g	Inductance of ac/grid side filter/transformer *(H)*.
ω_c	Switching frequency (rad/s). $\omega_c = 2\pi f_c$.
f_c	Switching frequency (Hz).
z	Intermediate variable. $z = \omega_c t + \theta_c$.
y	Intermediate variable $y = \omega_o t + \theta_x$.

Manuscript received February 16, 2021; revised July 13, 2021; accepted August 17, 2021. Date of publication September 1, 2021; date of current version November 30, 2021. This work was supported by the U.K. EPSRC Prosperity Partnership "A New Partnership in Offshore Wind under Grant EP/R004900/1." Recommended for publication by Associate Editor L. Peng. *(Corresponding author: Milijana Odavic.)*

The authors are with Electrical Machines and Drives Research Group, University of Sheffield, S1 4DE Sheffield, U.K. (e-mail: ssthakur1@sheffield.ac.uk; m.odavic@sheffield.ac.uk; ateyahmed79@gmail.com; z.q.zhu@sheffield.ac.uk; k.atallah@sheffield.ac.uk).

Color versions of one or more figures in this article are available at https://doi.org/10.1109/TPEL.2021.3108877.

Digital Object Identifier 10.1109/TPEL.2021.3108877

θ_c.	PWM carrier phase shift angle (rad).
$\theta_c^{r,k}$	PWM carrier phase shift angle of kth SM in upper/lower arm (rad).
θ_p	PWM carrier phase shift angle of the upper arm with respect to the lower arm (rad).
M_{pk}	Peak of the modulation signal.
m	Multiples of carrier frequency.
n	Multiples of fundamental frequency.
$J_k(u)$	Bessel function of kth order with argument u.
j	Imaginary part of complex number.
Re	Real part of complex number.
F	Number of negative-voltage states in the arm voltage.
t	Time (s).
T	Fundamental time period (s).
$\mathrm{round}()$	Round to nearest integer.
$\mathrm{ceil}()$	Round toward positive infinity (next higher integer).

I. INTRODUCTION

MODULAR multilevel converters (MMCs) are modular, efficient, provide better power quality, and easy scalability to medium and high voltages. MMCs are popular for high voltage direct current transmission, medium voltage drives and renewable energy storage systems [1]–[7]. Of the various submodule (SM) topologies of MMC, the half-bridge (HB) SM topology i.e., HB-MMC is most popular due to its lower device count. Numerous, publications have discussed the HB-MMC operation and steady-state modelling [8]–[11]. The major drawbacks of the HB-MMC are the lack of dc fault handling and ride through capability which have led to the research in alternative SM topologies [1]. Full-bridge sub module (FBSM) based MMC has gained popularity as it overcomes the abovementioned limitations of HB-MMC i.e., the converter can support the ac system with reactive power, control during dc faults for improved system stability. The FBSMs are sometimes referred to as bridge-cells, and the FB-MMC as double-star bridge-cell configuration [12]. The FBSM consists of a dc capacitor and four switching devices (IGBTs, MOSFETs, etc.) and can produce zero, positive and even negative output voltage switching states. For this reason, the FB-MMC can operate with arbitrary dc-link voltages and even achieve ac to ac direct power conversion [2], [12]. Thus, the FB-MMC can be also operated with zero and negative dc voltages, thereby facilitating operation even during dc side pole to pole or pole to ground faults [12], [13], [16]. However, the FB-MMC has twice the number of switching devices compared to the HB-MMC and thus suffers from increased size, cost, and losses. In recent works, the negative-voltage states of the FBSMs are also utilized under normal/healthy operation to improve the device utilization by increasing the converter modulation index and extending the ac output voltage range [17]. Moreover, the utilization of negative-voltage states not only extends the ac output voltage range but also facilitates operation of the FB-MMC with reduced dc voltages [12], [16], [18]. Recent studies also show that by choosing an appropriate converter modulation index by optimally utilizing the negative-voltage states, the energy variations in the arms are minimized significantly thereby reducing the energy storage requirement i.e., the SM capacitance [17], [19], [20]. The optimal modulation index varies with the operating power factor [19] and for converters operated near unity power factor the optimal modulation index is 1.414 [17], [20]. The energy storage requirement is further reduced by zero sequence voltage injection in [21] and [22] and by injecting appropriate circulating currents in [23] and [24].

To decrease the system cost and losses, hybrid MMCs; can be employed. These converters use a mixture of HB and FB SMs where the negative FBSM voltage states are introduced to enable dc fault blocking capability and higher ac voltages (or reduced dc voltages) [25], [26]. The HBSMs in the hybrid MMC require bipolar arm currents for successful voltage balancing and therefore limit the maximum modulation index [25]. Also, the different charging and discharging behavior of the FBSMs and the HBSMs leads to uneven loss distribution increasing the complexity of the SM capacitor voltage balancing algorithm [27]–[30]. On the contrary, the FB-MMCs have identical SMs and thus the SM capacitor voltage balancing is easily achieved. The FB-MMC can operate with reduced, zero and even negative dc voltages. For this reason, the FB-MMC gained popularity even though it has a higher device count than the hybrid converter.

Different modulation techniques are also investigated in literature to improve the performance of MMCs [1]. The most, commonly used modulation methods are nearest level control, staircase modulation, phase disposition modulation and phase shift carrier (PSC) modulation [16], [31]–[39]. The PSC pulsewidth modulation (PWM) is widely adopted for medium voltage MMCs as it brings many benefits such as: high resultant switching frequency and a low total harmonic distortion (THD), and even voltage stress and loss distribution among the cascaded SMs making the SM capacitor voltage balancing easier [11], [40]–[44]. The PSC-PWM for FBSM MMCs is investigated in [40] and [44]. However, the analysis is limited to FB-MMC operation without utilizing the negative-voltage states where the FB-MMC is operated and designed similar to a HB-MMC (referred to as "buck-mode" in this article). Operation of FB-MMC utilizing the negative-voltage states to boost the ac voltage (or to reduce the dc voltage) is hereon referred to as boost mode. Allu *et al.* [45], [46] used simulations to first demonstrate that the modulation index in boost mode not only affects the arm energy variations i.e., SM capacitor voltage ripple but also the THD of the output voltage. However, a detailed analysis of the harmonic features, of FB-MMC operating in boost mode is not reported in the literature.

So far, very few studies have analyzed the principles of PSC-PWM for FB-MMC operating in boost mode. It is still not clear how the boost mode affects the harmonic characteristics of the FB-MMC and moreover, how the harmonics in the output voltage could be minimized. The effect of the upper and the lower arm carrier phase shift angle is also, not fully understood. Therefore, the aim of this article is to provide the analytical harmonic model of output voltage of FB-MMC with PSC-PWM operated in boost mode. Further, the model is utilized to

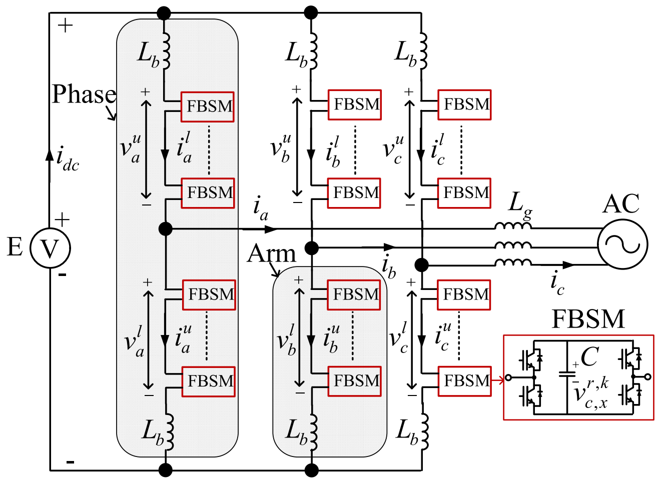

Fig. 1. Schematic block diagram of FB-MMC.

investigate the impact the of the number of SMs, the modulation index and the upper/lower arm carrier phase angle on the output voltage harmonics. The optimal design criteria to minimize the FB-MMC output voltage harmonics are then proposed.

The rest of this article is organized as follows. The basic operating principles of FB-MMC are introduced in Section II. The PSC-PWM for FB-MMC in boost mode is explained in Section III. The new analytical harmonic model is given in Section IV and the criteria for the output voltage harmonic minimization is explained in Section V. The simulation results and harmonic analysis are presented in Section VI. The experimental results are given in Section VII. Section VIII presents discussion on boost mode, comparison with the most recent approach in the literature and the effect of SM capacitor voltage ripple on the harmonic spectrum. Section IX concludes the article.

II. BASIC OPERATING PRINCIPLES OF FB-MMC

A. *Structure of FB-MMC*

The schematic of FB-MMC is shown in Fig. 1. The FB-MMC consists of three phases each with an upper arm and a lower arm. Each arm of the converter comprises N cascaded FBSMs and each FBSM comprises a dc capacitor and four insulated gate bipolar transistors.

B. *Mathematical Model of FB-MMC*

Assuming balanced steady-state operation, the cascaded FBSMs are identical and can be represented by an equivalent controllable voltage source corresponding to each arm. Thus, the single phase equivalent average model is derived as shown Fig. 2. The following equations can be obtained by Kirchhoff's voltage-law:

$$R_b i_x^u + L_b \frac{di_x^u}{dt} = \frac{E}{2} - v_x^u - R_g i_x - L_g \frac{di_x}{dt} - v_{gx} \tag{1a}$$

$$R_b i_x^l + L_b \frac{di_x^l}{dt} = \frac{E}{2} - v_x^l + R_g i_x + L_g \frac{di_x}{dt} + v_{gx}. \tag{1b}$$

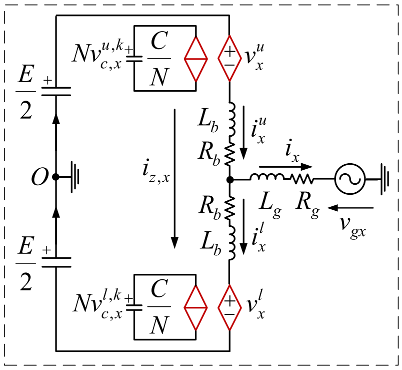

Fig. 2. Single phase average model of FB-MMC.

The ac/load current is split equally between the two arms in balanced operation. If the arm currents are controlled such that there are no harmonics in the circulating current, the arm currents are expressed as [47]

$$i_x^u = \frac{I_m}{4} k_m \text{Cos}\left(\phi_m\right) + \frac{I_m \text{Cos}\left(\omega_o t + \theta_x + \phi_m\right)}{2} \tag{2a}$$

$$i_x^l = \underbrace{\frac{I_m}{4} k_m \text{Cos}\left(\phi_m\right)}_{\text{dc component } (i_{\text{dc}})} - \underbrace{\frac{I_m \text{Cos}\left(\omega_o t + \theta_x + \phi_m\right)}{2}}_{\text{ac component}} \tag{2b}$$

where the converter modulation index k_m is

$$k_m = \frac{2V_m}{E}. \tag{3}$$

Using (1)–(3), the arm voltages can be expressed as

$$v_x^u = \frac{E}{2} - \left(R_b i_{z,x} + L_b \frac{di_{z,x}}{dt}\right) - v_{mx} \tag{4a}$$

$$v_x^l = \frac{E}{2} - \left(R_b i_{z,x} + L_b \frac{di_{z,x}}{dt}\right) + v_{mx} \tag{4b}$$

where the MMC fundamental phase voltage is

$$v_{mx} = \left(\left(\frac{R_b}{2} + R_g\right) i_x + \left(\frac{L_b}{2} + L_g\right) \frac{di_x}{dt} + v_{gx}\right). \tag{5}$$

Here, the MMC fundamental phase voltages and currents are represented as

$$v_{mx} = V_m \text{ Cos}\left(\omega_o t + \theta_x\right) \tag{6a}$$

$$i_x = I_m \text{ Cos}\left(\omega_o t + \theta_x + \phi_m\right) \tag{6b}$$

where V_m is the amplitude of the fundamental MMC phase voltage.

C. *Boost Mode Operation of FB-MMC*

Neglecting the voltage drop in the arm inductors, the voltage in the upper/lower arm from (4) and (6a) is expressed as

$$v_x^u = \left(\frac{E}{2} - V_m \text{Cos}\left(\omega_o t + \theta_x\right)\right) \tag{7a}$$

$$v_x^l = \left(\frac{E}{2} + V_m \text{Cos}\left(\omega_o t + \theta_x\right)\right). \tag{7b}$$

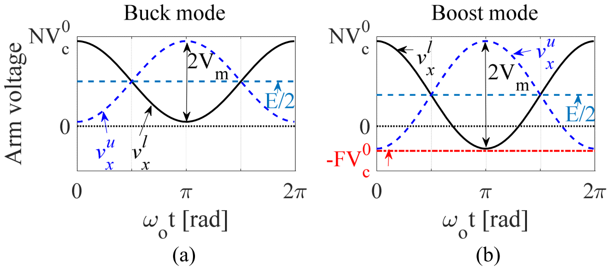

Fig. 3. Arm voltages, ac fundamental voltage, and dc voltage. (a) Buck mode. (b) Boost mode.

The arm voltage is composed of a dc component and a fundamental component. In the buck mode of operation where the negative-voltage states of the FBSMs are not used, the range of the arm voltage is limited to $0\ to\ NV_c^0$, where V_c^0 is the average SM capacitor voltage. Here, the amplitude of the ac-side voltage is limited to $V_m \leq NV_c^0/2$ and is lower than the dc side voltage with $E/2 = NV_c^0/2$ as depicted in Fig. 3(a) and thus, the converter modulation index is limited to $k_m \leq 1$ i.e., $V_m \leq (E/2)$. The boost mode operation is depicted in Fig. 3(b), As an example, out of the N FBSMs, F FBSMs are allowed to operate with negative-voltage states. The range of the arm voltage is now extended to $-FV_c^0\ to\ NV_c^0$. This way, the amplitude of the ac voltage is extended to $V_m \leq (N+F)V_c^0/2$ and is higher than the dc voltage with $E/2 = (N-F)\ V_c^0/2$ thereby extending the converter operation to $k_m > 1$ and $V_m > (E/2)$.

D. Variation of Arm Energy and SM Capacitor Voltage Ripple in Boost Mode

The instantaneous arm energy in the FB-MMC is given by the product of the arm current and the arm voltage and is expressed as [20]

$$\boldsymbol{e_x^r} = \int \underbrace{\boldsymbol{p_x^r}}_{\textbf{instantaneous arm power}} \boldsymbol{dt} = \int (\boldsymbol{v_x^r}.\boldsymbol{i_x^r})\ \boldsymbol{dt}$$

$$= \underbrace{\frac{3}{2}V_m I_m}_{\text{apparent power}} \left[\underbrace{\mp\left(\begin{array}{r} -\frac{\text{Sin}(\omega_o t+\theta_x+\phi_m)}{3k_m\omega_o} \\ +\frac{k_m\text{Cos}(\phi_m)\text{Sin}(\omega_o t+\theta_x)}{6\omega_o} \end{array} \right)}_{\text{fundamental frequency ripple}} \underbrace{+\left(\frac{\text{Sin}\left(2\left(\omega_o t+\theta_x\right)+\phi_m\right)}{12\omega_o} \right)}_{\text{second harmonic ripple}} \right] \tag{8}$$

where "-" sign in the fundamental frequency ripple term is for the upper arm $(r = u)$ and "+" sign for the lower arm $(r = l)$. The output phase voltage amplitude is V_m, phase current amplitude is I_m and the current phase angle is ϕ_m. The converter modulation index is k_m ($k_m = 2V_m/E$, E is dc side voltage). The peak–peak arm energy ripple is given by

$$\Delta e = \left(\max\left(e_x^r\right) - \min\left(e_x^r\right)\right) \quad t \in [0, T]\,. \tag{9}$$

The relation between the arm energy ripple and the SM capacitor voltages is given by

$$v_{c,x}^{r,k} = \underbrace{V_c^0}_{\text{dc value}} + \underbrace{\frac{e_x^r}{NCV_c^0}}_{\text{voltage ripple}}$$

$$= V_c^0 + \frac{3V_m I_m}{2NCV_c^0} \left[\underbrace{\mp\left(\begin{array}{r} -\frac{\text{Sin}(\omega_o t+\theta_x+\phi_m)}{3k_m\omega_o} \\ +\frac{k_m\text{Cos}(\phi_m)\text{Sin}(\omega_o t+\theta_x)}{6\omega_o} \end{array} \right)}_{\text{fundamental component}} \underbrace{+\left(\frac{\text{Sin}\left(2\left(\omega_o t+\theta_x\right)+\phi_m\right)}{12\omega_o} \right)}_{\text{second harmonic}} \right]. \tag{10}$$

Further, the peak–peak SM capacitor voltage ripple (%) is given by

$$\Delta V_c\ (\%) = \frac{\left(\max\left(v_{c,x}^{r,k}\right) - \min\left(v_{c,x}^{r,k}\right)\right)}{V_c^0} \times 100\%\ t \in [0, T] \tag{11}$$

which further simplifies to (12) using (9)–(11), given by

$$\Delta V_c\ (\%) = \frac{\Delta \text{e}}{NC(V_c^0)^2} \times 100\%. \tag{12}$$

The variation of Δe (per unit) with the modulation index k_m is shown in Fig. 4(a) for the unity power factor condition. As the modulation index is increased from the conventional $k_m = 0.9$ ($\Delta e = 1$p.u., buck mode), the arm energy ripple first decreases and reaches the minimum of $\Delta e \sim 0.33$ p.u. at $k_m = 1.41$, before increasing again for $k_m > 1.4$. As the peak-peak SM capacitor voltage ripple ΔV_c is directly proportional to Δe [as can be seen from (12)], the ΔV_c also reaches its minimum at $k_m = 1.4$ ($\Delta V_c \sim 0.5$ p.u.) for the fixed SM capacitance and in relation to the V_c^0 [see Fig. 4(c)]. For this analysis, the ac side voltage is assumed to be fixed, the dc side voltage is reduced to increase the modulation index, and the dc SM capacitor voltage V_c^0 is appropriately reduced to keep the ac side voltage constant [46], these are shown in Fig. 4(c). Therefore, by operating the FB-MMC at optimal k_m (boost mode) the SM capacitor voltage ripple is reduced greatly. On the other hand, if the SM capacitor voltage ripple is kept the same in both buck and boost modes, the SM capacitance can be drastically reduced.

III. PSC MODULATION FOR FB-MMC IN BOOST MODE

A. Modulation Signal

Assuming balanced steady-state operation with identical SMs in each arm, the arm voltage (7) is equally divided across the SMs where the output voltage of each SM in the upper/lower arm is expressed as

$$v_x^{u,k} = \frac{1}{N}\left(\frac{E}{2} - V_m\text{Cos}\left(\omega_o t + \theta_x\right)\right) \tag{13a}$$

$$v_x^{l,k} = \frac{1}{N}\left(\frac{E}{2} + V_m\text{Cos}\left(\omega_o t + \theta_x\right)\right). \tag{13b}$$

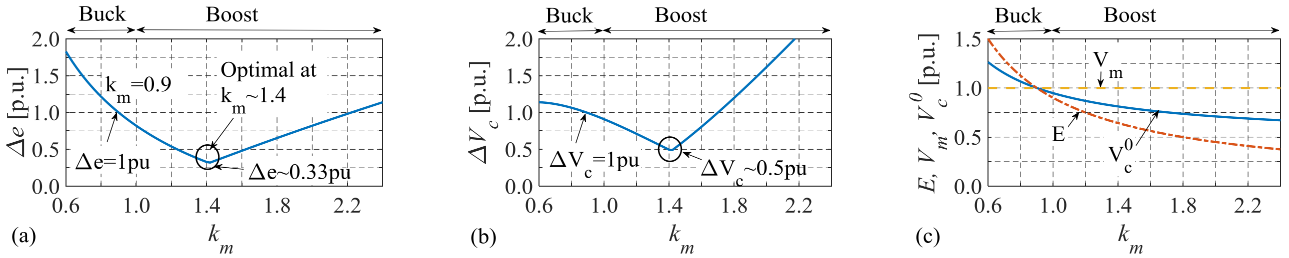

Fig. 4. Variation of (a) arm energy ripple Δe. (b) SM capacitor voltage ripple ΔV_c. (c) V_m , E, and V_c^0, with modulation index k_m at unity power factor.

The SM capacitor voltage ripple (which is further reduced in boost mode) is neglected for simplicity and the SM capacitor voltages are assumed to be pure dc (i.e., $v_{c,x}^{r,k} \sim V_c^0$) under the assumption that the SM capacitance is large enough to limit the capacitor voltage ripple within 10% [40]. The modulation signal of each FBSM can be expressed as

$$M_x^{u,k} = v_x^{u,k} \;/V_c^0 \tag{14a}$$

$$M_x^{l,k} = v_x^{l,k}/V_c^0. \tag{14b}$$

Further simplifying (14) using (13), the modulation signal of each SM is given by

$$M_x^{u,k} = \frac{M_0}{2} + \frac{M_1}{2}\mathrm{Cos}\left(\omega_o t + \theta_x + \pi\right) \tag{15a}$$

$$M_x^{l,k} = \frac{M_0}{2} + \frac{M_1}{2}\mathrm{Cos}\left(\omega_o t + \theta_x\right) \tag{15b}$$

where the dc modulation component M_0 and the amplitude of the fundamental modulation component M_1 are defined as [46]

$$M_0 = E/NV_c^0 \tag{16a}$$

$$M_1 = \frac{2V_m}{NV_c^0}\,. \tag{16b}$$

Here, boost mode is when $2V_m > E$ which translates to $M_1 > M_0$ i.e., the modulation signal (15) crosses the zero axis and is negative. The average SM capacitor voltage is chosen such that the peak of the modulation signal is limited to $0 \leq M_{pk} \leq 1$ for linear operation of the MMC and is expressed as

$$V_c^0 = \frac{E/2 + V_m}{NM_{\mathrm{pk}}}. \tag{17}$$

where the peak of the modulation signal is

$$M_{pk} = \frac{M_1}{2} + \frac{M_0}{2}. \tag{18}$$

The peak modulation is generally kept high for better device utilization.

B. Implementation of PSC-PWM

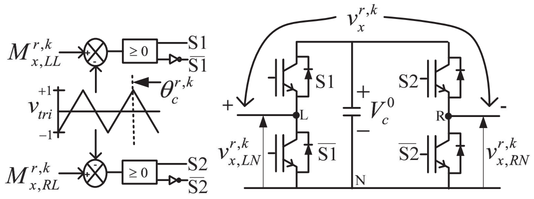

Fig. 5. Three-level pulse width modulation of FBSM.

Like the single-phase inverters, the FBSMs can be either operated in two-level PWM or three-level PWM. The three-level modulation also known as unipolar modulation is used in this article as it has higher effective output switching frequency of two times the device switching frequency and is therefore widely adopted [48]. A single triangular carrier and two modulation signals are used per SM (see Fig. 5) with each modulation signal corresponding to the left-leg (LL) and the right-leg (RL) of SM [46]. Double edge naturally sampled modulation is assumed in this article. The modulation signal is compared with the triangular carrier wave to generate the switching pulses for the corresponding left/right leg. The individual modulation signals for the LL and the RR in upper/lower arm SMs are given by

$$M_{x,\mathrm{LL}}^{u,k} = \frac{1}{2} + \frac{M_0}{4} + \frac{M_1}{4}\mathrm{Cos}\left(\omega_o t + \theta_x + \pi\right) \tag{19a}$$

$$M_{x,\mathrm{RL}}^{u,k} = \frac{1}{2} - \frac{M_0}{4} - \frac{M_1}{4}\mathrm{Cos}\left(\omega_o t + \theta_x + \pi\right) \tag{19b}$$

$$M_{x,\mathrm{LL}}^{l,k} = \frac{1}{2} + \frac{M_0}{4} + \frac{M_1}{4}\mathrm{Cos}\left(\omega_o t + \theta_x\right) \tag{19c}$$

$$M_{x,\mathrm{RL}}^{l,k} = \frac{1}{2} - \frac{M_0}{4} - \frac{M_1}{4}\mathrm{Cos}\left(\omega_o t + \theta_x\right). \tag{19d}$$

The triangular carriers of each SM in an arm are phase shifted by an angle π/N which is optimaly chosen to shift the effective arm switching frequency to N times of SM switching frequency [16], [40], [44], [48]. The carrier phase shift angle of kth SM in the upper and the lower arm is given by

$$\theta_c^{u,k} = \theta_p + \frac{\pi}{N}\left(k-1\right) \tag{20a}$$

$$\theta_c^{l,k} = \frac{\pi}{N}\;\left(k-1\right) \tag{20b}$$

where θ_p is the PWM carrier phase shift angle of the upper arm with respect to the lower arm. The angle θ_p has significant impact on the harmonic distribution of the MMC output voltage and will be discussed in the following sections.

The PSC-PWM is demonstrated for the buck mode and boost mode in Fig. 6 for $N = 4$. It can be observed that the SM output voltage has zero and positive levels in the buck mode as depicted in Fig. 6(a), whereas in boost mode the SM output voltage has

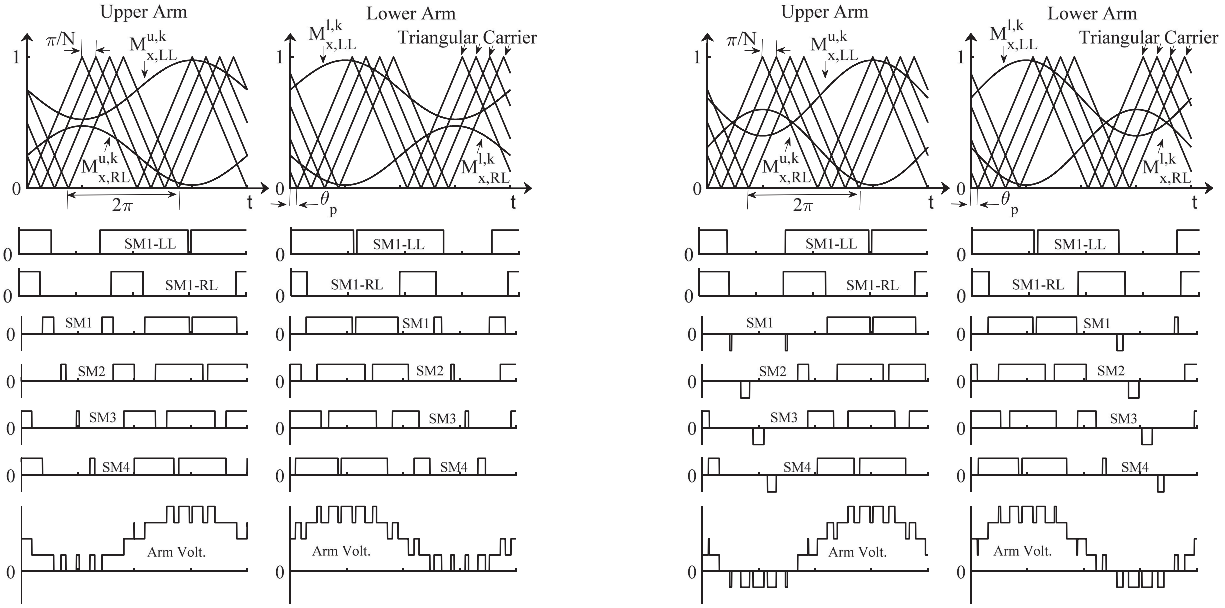

(a) (b)

Fig. 6. PSC-PWM for FBSM MMCs ($N = 4, \;\; f_c = 2f_o$). (a) Buck mode. (b) Boost mode.

zero, positive and negative levels as depicted in Fig. 6(b). As such, the arm voltage, has only zero and positive voltage levels in the buck mode and has zero, positive and negative-voltage levels in boost mode. Thus, the ac side voltage, is higher in boost mode as compared to the buck mode for similar SM capacitor voltages. The negative-voltage levels in the arm voltage (4) [or the modulation signal (15)] correspond to the region where the LL and RL modulation signals (19) overlap signifying boost mode as shown in Fig. 6(b).

IV. HARMONIC CHARACTERIZATION OF FB-MMC

A. SM Output Voltage

Assuming balanced steady-state with identical dc SM capacitor voltages of V_c^0 and modulation signal (19), and representing the SM, LL, and RL output voltages in the general carrier-based PWM form given by (A0) [48], the LL and RL harmonic coefficients are given by

$$C^{\mathrm{LL}}_{m,n} = \frac{1}{2\pi^2}\int_{-\pi}^{\pi}\int_{-\pi\left(M^{r,k}_{x,LL}\right)}^{\pi\left(M^{r,k}_{x,LL}\right)} V_c^0 e^{j(mz+ny)} dz\, dy \tag{21a}$$

$$C^{\mathrm{RL}}_{m,n} = \frac{1}{2\pi^2}\int_{-\pi}^{\pi}\int_{-\pi\left(M^{r,k}_{x,RL}\right)}^{\pi\left(M^{r,k}_{x,RL}\right)} V_c^0 e^{j(mz+ny)} dz\, dy. \tag{21b}$$

For simplicity, the SM capacitor voltage ripple is neglected and the SM capacitor voltages are assumed to be pure dc [40]. Solving (21), the analytical harmonic spectrum of LL and RL output voltages in the lower arm SMs are given by

$$\begin{aligned} v^{l,k}_{x,LN} &= V_c^0\left(\frac{1}{2}+\frac{M_0}{4}\right)+\frac{V_c^0 M_1}{4}\cos(y) \\ &\quad + \mathrm{Re}\sum_{m=1}^{\infty}\sum_{n=-\infty}^{\infty} \mathrm{e}^{-j(ny+mz)} \\ &\quad \times\left[\frac{2V_c^0}{m\pi}J_n\left(mM_1\frac{\pi}{4}\right)\sin\left(\left(m\left(1+\frac{M_0}{2}\right)+n\right)\frac{\pi}{2}\right)\right] \end{aligned} \tag{22a}$$

$$\begin{aligned} v^{l,k}_{x,RN} &= V_c^0\left(\frac{1}{2}-\frac{M_0}{4}\right)-\frac{V_c^0 M_1}{4}\cos(y) \\ &\quad + \mathrm{Re}\sum_{m=1}^{\infty}\sum_{n=-\infty}^{\infty} \mathrm{e}^{-j(ny+mz)} \\ &\quad \times\left[\frac{2V_c^0}{m\pi}J_n\left(-mM_1\frac{\pi}{4}\right)\sin\left(\left(m\left(1-\frac{M_0}{2}\right)+n\right)\frac{\pi}{2}\right)\right]. \end{aligned} \tag{22b}$$

The SM output voltage in the lower arm is given by $v_x^{r,k} = v^{r,k}_{x,LN} - v^{r,k}_{x,RN}$ which simplifies to (see Appendix A)

$$\begin{aligned} v^{l,k}_{x} &= V_c^0\left(\frac{M_0}{2}\right)+\frac{V_c^0 M_1}{2}\cos(\omega_o t+\theta_x) \\ &\quad + \mathrm{Re}\sum_{m=1}^{\infty}\sum_{n=-\infty}^{\infty} e^{-j\left(n(\omega_o t+\theta_x)+2m\left(\omega_c t+\theta_c^{l,k}\right)\right)} \\ &\quad \mathrm{x}\left[\frac{2V_c^0}{m\pi}J_n\left(mM_1\frac{\pi}{2}\right)\cos(m\pi)\, sin\left((mM_0+n)\frac{\pi}{2}\right)\right]. \end{aligned} \tag{23a}$$

Similarly, the SM output voltage in the upper arm is given by

$$v^{u,k}_{x} = V_c^0\left(\frac{M_0}{2}\right)-\frac{V_c^0 M_1}{2}\cos(\omega_o t+\theta_x) \tag{23b}$$

$$+\,\mathrm{Re}\sum_{m\,=\,1}^{\infty}\sum_{n\,=\,-\infty}^{\infty} e^{-j\left(n(\omega_o t+\theta_x+\pi)+2m\left(\omega_c t+\theta_c^{u,k}\right)\right)}$$
$$\times\left[\frac{2V_c^0}{m\pi}J_n\left(mM_1\frac{\pi}{2}\right)\cos\left(m\pi\right)\sin\left(\left(mM_0+n\right)\frac{\pi}{2}\right)\right].$$

B. Arm Voltage

Using (20) and (23) and further simplifying the arm voltages are given by (24a) and (24b), respectively, [see Appendix (A4)]

$$v_x^l=\sum_{k=1}^{N}v_x^{l,k}\;=\frac{NM_0V_c^0}{2}\;,+\frac{NM_1V_c^0}{2},\cos\left(\omega_o t+\theta_x\right)$$
$$+\,\mathrm{Re}\sum_{m\,=\,1}^{\infty}\sum_{n\,=\,-\infty}^{\infty} e^{-j(n(\omega_o t+\theta_x)+2mN\omega_c t)}$$
$$\times\left[\frac{2V_c^0}{m\pi}J_n\left(mNM_1\frac{\pi}{2}\right)\cos\left(mN\pi\right)\sin\left(\left(mNM_0+n\right)\frac{\pi}{2}\right)\right] \tag{24a}$$

$$v_x^u=\sum_{k=1}^{N}v_x^{u,k}\;=\frac{NM_0V_c^0}{2}\;-\frac{NM_1V_c^0}{2}\cos\left(\omega_o t+\theta_x\right)$$
$$+\,\mathrm{Re}\sum_{m\,=\,1}^{\infty}\sum_{n\,=\,-\infty}^{\infty} e^{-j(n(\omega_o t+\theta_x+\pi)+2mN(\omega_c t+\theta_p))}$$
$$\times\left[\frac{2V_c^0}{m\pi}J_n\left(mNM_1\frac{\pi}{2}\right)\cos\left(mN\pi\right)\sin\left(\left(mNM_0+n\right)\frac{\pi}{2}\right)\right]. \tag{24b}$$

C. Output Voltage

Using (24), the PWM output voltage v_{ox} simplifies to

$$v_{ox}=\frac{v_x^l-v_x^u}{2}\;=\frac{NM_1V_c^0}{2}\;\cos\left(\omega_o t+\theta_x\right) \tag{25}$$
$$+\,\mathrm{Re}\sum_{m\,=\,1}^{\infty}\sum_{n\,=\,-\infty}^{\infty} e^{-j(n(\omega_o t+\theta_x)+2mN\omega_c t)}$$
$$\times\left[\frac{1-e^{-j(n\pi+2mN\theta_p)}}{2}\right]$$
$$\times\left[\frac{2V_c^0}{m\pi}J_n\left(mNM_1\frac{\pi}{2}\right)\cos\left(mN\pi\right)\sin\left(\left(mNM_0+n\right)\frac{\pi}{2}\right)\right].$$

Further simplifying, the PWM output voltage is expressed as

$$v_{ox}=\frac{v_x^l-v_x^u}{2}\;=\frac{NM_1V_c^0}{2}\;\cos\left(\omega_o t+\theta_x\right) \tag{26}$$
$$+\sum_{m\,=\,1}^{\infty}\sum_{n\,=\,-\infty}^{\infty}$$
$$\mathrm{Sin}\left(\left(n\left(\omega_o t+\theta_x\right)+2mN\omega_c t\right)+\frac{\left(n\pi+2mN\theta_p\right)}{2}\right)$$
$$\times\left[\frac{2V_c^0}{m\pi}J_n\left(mNM_1\frac{\pi}{2}\right)\cos(mN\pi)\sin\left(\left(mNM_0+n\right)\frac{\pi}{2}\right)\right]$$
$$\times\left[\sin\left(\frac{n\pi+2mN\theta_p}{2}\right)\right].$$

V. OUTPUT VOLTAGE HARMONIC MINIMIZATION

Output voltage with lower harmonic distortion means smaller and cheaper output filters. It is therefore beneficial to minimize the harmonics in the output voltage, especially the harmonics in the first high frequency carrier group ($m\;=\;1$) which mainly defines the filter requirement. To study the impact of the dc side and ac side voltage selection (i.e., input/output voltage ratio) on the harmonic spectrum, it is sufficient to analyze the harmonics for different modulation parameters M_0 and M_1 as these are related to the dc and ac side voltages (16). The order $\{m, n\}$ of the nonzero harmonics in (26) is defined by the terms $\sin((mNM_0+n)\frac{\pi}{2})$ and $(\sin(\frac{n\pi+2mN\theta_p}{2}))$ which in turn depends on N, $M_{0,}$ and θ_p. Note the amplitude of the fundamental modulation component M_1 affects the amplitude of the harmonics in (26) whereas the order of the non-zero harmonics is predominantly defined by N, M_0 and θ_p.

A. Complete Harmonic Elimination at $m\;=\;1$

It is seen from (26) that all the harmonics at $m\;=\;1$ are zero when the product $\sin((mNM_0+n)\frac{\pi}{2})$ x $(\sin(\frac{n\pi+2mN\theta_p}{2}))$ is zero. For N x $M_0=$ even (or odd) the term $\sin((mNM_0+n)\frac{\pi}{2})$ at $m=1$ is nonzero for n $=$ odd (or even). These harmonics can be eliminated from the output voltage by making the term $(\sin(\frac{n\pi+2mN\theta_p}{2}))$ zero for $n\;=$ odd (or even) by choosing $\theta_p=H_1\;\pi/2N$ (*or* $\theta_p=H_2\;\pi/2N$) where $H_1=\;\pm1,\pm3,\ldots,$ (*or* $H_2=\;0,\pm2,\pm4,\ldots,$). Based on this, the optimal angle is $\theta_p=\;\pi/2N$ (with $H_1=\;1$) for N $M_0=$ even and $\theta_p=\;0$ (with $H_2=\;0$) for N $M_0=$ odd. This can be summarized as

$$\begin{aligned} v_{ox}&=\;0 \text{ at } m\;=\;1 \text{ for}\\ \theta_p&=\;0,\;\{(N \text{ x } M_0) \text{ is odd}\\ \theta_p&=\frac{\pi}{2N},\;\{(N \text{ x } M_0) \text{ is even.}\end{aligned} \tag{27}$$

Alternatively, (27) can also be written as

$$v_{ox}=\;0 \text{ at } m\;=\;1 \text{ for} \tag{28}$$
$$\theta_p=\;0,\quad\left\{N \text{ is odd and } M_0=\tfrac{K}{N},\text{ where } K\;=\;1,3,5\ldots N\right.$$
$$\theta_p=\frac{\pi}{2N},$$
$$\begin{cases}N \text{ is odd and } M_0=\frac{K}{N}, \text{ where } K\;=\;2,4,6\ldots(N-1)\\ N \text{ is even and } M_0=\frac{K}{N}, \text{ where } K\;=\;1,2,3\ldots N.\end{cases}$$

Therefore, by appropriate selection of N, $M_{0,}$ and θ_p as given by (28) the frequency of the lowest harmonic group in the output voltage changes from $2Nf_c$ to $4\,Nf_c$ ($m\;=\;2$) thereby doubling

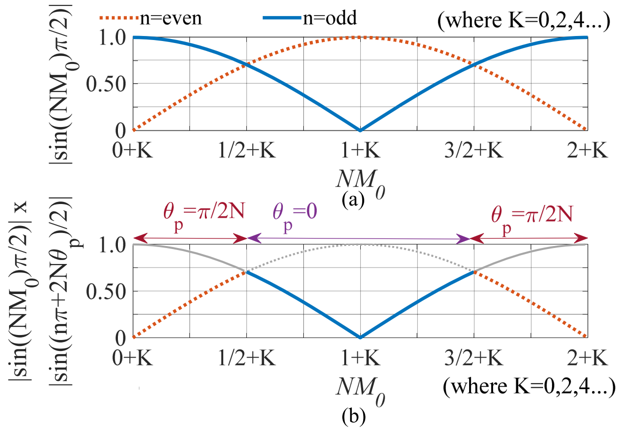

Fig. 7. (a) Variation of even and odd harmonics in the output voltage. (b) Selection of optimal θ_p.

the filter-cutoff frequency and significantly reducing the filter size.

B. Harmonic Minimization At $m = 1$

When N x M_0 is not an integer i.e., neither odd nor even but N x M_0 is a fraction, under these conditions, the term $\sin((mNM_0 + n)\frac{\pi}{2})$ in (26) is non zero for all $n = 0, \pm1, \pm2, \ldots$ at $m = 1$. Complete harmonic elimination therefore cannot be achieved at $m = 1$ as θ_p can either eliminate $n =$ even or $n =$ odd harmonics. On the other hand, harmonics at $m = 1$ can be minimized by eliminating $n =$ even or $n =$ odd harmonics whichever are of higher amplitude. A generalized solution and analysis can be made based on the (periodic) variation of $|\sin((NM_0 + n)\frac{\pi}{2})|$ in (26) with (NM_0) as shown in Fig. 7(a) for $n =$ odd and $n =$ even. The relative amplitude variation of $|\sin((NM_0 + n)\frac{\pi}{2})|$ with $n =$ odd and $n =$ even is used to determine the selection of θ_p. The optimal θ_p selection for minimum harmonic amplitudes is demonstrated in Fig. 7(b), which shows the variation of $|\sin((NM_0 + n)\frac{\pi}{2})|$ x $|(\sin(\frac{n\pi+2mN\theta_p}{2}))|$. Here, the $n =$ odd harmonics are larger in amplitude in the range $(0 + K) \le NM_0 \le (1/2 + K)$ and $(3/2 + K) \le NM_0 \le (2 + K)$ (where $K = 0, 2, 4\ldots$) and therefore eliminated from the output voltage by choosing $\theta_p = \pi/2N$. Similarly, the $n =$ even harmonics are larger in amplitude in the range $(1/2 + K) \le NM_0 \le (3/2 + K)$ (where $K = 0, 2, 4\ldots$) and therefore eliminated from the output voltage by choosing $\theta_p = 0$. The optimal angle θ_p for harmonic minimization is summarized as

The expression (29) shown at bottom of next page, can be further simplified as

$$\begin{aligned} v_{ox} &= \text{minimum at } m = 1 \text{ for} \\ \theta_p &= 0 \ \{\text{nearest integer } to \ (N \text{ x } M_0) \ \text{ is odd} \\ \theta_p &= \tfrac{\pi}{2N}, \ \ \{\text{nearest integer to } (N \text{ x } M_0) \ \text{ is even.} \end{aligned} \tag{30}$$

In conclusion, for N x $M_0 =$ fraction, the lowest harmonic group in the output voltage is still $2Nf_c$ $(m = 1)$. However, as the harmonics at $m = 1$ (dominant) are reduced, the required filter size is minimized by choosing the optimal angle θ_p given by (30).

C. Optimal Upper/Lower Arm Carrier Phase Shift Angle

Combining (27) and (30), the optimal angle θ_p is expressed as

$$\begin{aligned} \theta_p &= 0, \ \{\text{round}\,(N \text{ x } M_0) \ \text{ is odd} \\ \theta_p &= \frac{\pi}{2N}, \ \ \{\text{round}\,(N \text{ x } M_0) \ \text{ is even} \end{aligned} \tag{31}$$

where the function round() is round to nearest integer. Here, the effective switching frequency of the output voltage is $4Nf_c$ for N x $M_0 =$ integer and is $2Nf_c$ for N x $M_0 =$ fraction.

D. Analytical Verification

The efficacy of (31) [(27) and (30)] is verified in Fig. 8, which shows the variation of the rms amplitude of the harmonics $v_{ox}^{\{1,n\}}$ at $m = 1$ for certain cases of N, M_0 and θ_p, where the rms voltage $v_{ox}^{\{1,n\}}$ is defined as

$$v_{ox}^{\{1,n\}} = \sqrt{\sum_{n=-20}^{n=20} \left(\begin{array}{c} \frac{2V_c^0}{\pi} J_n\left(NM_1\frac{\pi}{2}\right)\cos\left(N\pi\right) \\ \text{x } \sin\left((NM_0 + n)\,\frac{\pi}{2}\right)\sin\left(\frac{n\pi+2N\theta_p}{2}\right) \end{array} \right)^2}. \tag{32}$$

Theoretically n is given by $-\infty \le n \le \infty$, however due to the nature of the Bessel function the first 10 to 20 harmonic orders are sufficient and thus $-20 \le n \le 20$ is used in this article. For the analysis in Fig. 8, the boost mode is obtained by assuming fixed ac-side voltage and reducing the dc voltage with the dc SM capacitor voltage defined by (17) and the individual modulation parameters defined by (16). The variation of $v_{ox}^{\{1,n\}}$ with N, M_0, and θ_p is shown in Fig. 8(a) and the corresponding variation in dc and ac voltages, and fundamental modulation amplitude is shown in Fig. 8(b). Here, the amplitude of the fundamental modulation signal component is varied as $M_1 = (2M_{\text{pk}} - M_0)$ (18) with $M_{\text{pk}} = 0.9$.

$$\begin{aligned} v_{ox} &= \text{minimum at } m = 1 \text{ for} \\ \theta_p &= 0, \left\{ \frac{1}{2} + K \le NM_0 \le \frac{3}{2} + K, \text{ where } K = 0, 2, 4, 6 \right. \\ \theta_p &= \frac{\pi}{2N}, \ \left\{ \begin{array}{l} 0 + K \le NM_0 \le \frac{1}{2} + K, \text{ where } K = 0, 2, 4, 6\ldots \\ \frac{3}{2} + K \le NM_0 \le 2 + K, \text{ where } K = 0, 2, 4, 6\ldots \end{array} \right. \end{aligned} \tag{29}$$

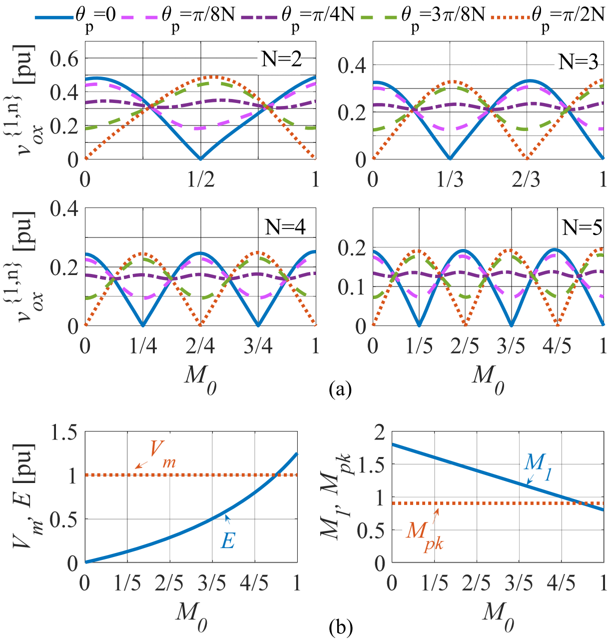

Fig. 8. (a) Variation of the voltage $v_{ox}^{\{1,n\}}$ with N, M_0, and θ_p ($M_{pk} = 0.9$). (b) Variation of E, V_m, and M_1 with $M_{pk} = 0.9$.

From Fig. 8(a), complete harmonic elimination at $m = 1$ is achieved with the rms value of the first group of harmonics $v_{ox}^{\{1,n\}} = 0$ for $\theta_p = 0$ at $N\ M_0 =$ odd and $\theta_p = \pi/2N$ at $N\ M_0 =$ even, as defined by (27). Further, $v_{ox}^{\{1,n\}}$ (32) is minimum for $\theta_p = 0$ at round $(NM_0) =$ odd and $\theta_p = \pi/2N$ at round $(NM_0) =$ even as given by (30) (31). The minor variations in the cross-over of $\theta_p = 0$ and $\theta_p = \pi/2N$ in Fig. 8 can be noticed when compared with Fig. 7 due to the nonlinear variation of the individual harmonic amplitudes and their rms. Nevertheless, for simplicity these can be neglected and the optimal θ_p is chosen as (30) and (31). It can also be seen from Fig. 8 that harmonic minimization is only achieved with $\theta_p = 0$ or $\theta_p = \pi/2N$, while other values of θ_p, such as $\theta_p = \frac{\pi}{8N}$, $\theta_p = \frac{\pi}{4N}$, and $\theta_p = \frac{3\pi}{8N}$ fail to achieve harmonic minimization, as expected from (26).

VI. HARMONIC ANALYSIS AND SIMULATIONS

Simulations are performed in MATLAB/Simulink to validate the analytical model and analyze the harmonic spectra for different design scenarios. The SM capacitor voltages are assumed to be ideal dc. The PSC-PWM pulses are generated as shown in Figs. 5 and 6. Three different scenarios are considered with $N = 5$, as $M_1 = 1.0$, $M_0 = 0.8$ $(= 4/5)$, $M_1 = 1.05$, $M_0 = 0.75$ $(= 3/4)$, and $M_1 = 1.2$, $M_0 = 0.6$ $(= 3/5)$. Each of these correspond to modulation index (voltage) ratio M_1/M_0 of 1.25, 1.4, and 2, respectively.

A. Harmonic Analysis

The time-domain waveforms and the extracted harmonic spectrum for $M_1 = 1.0$, $M_0 = 0.8$ $(= 4/5)$ are shown in Fig. 9. As expected, the SM voltage and the arm voltage utilize the negative-voltage states with the FB-MMC operating in boost mode. The harmonic spectra of the time-domain waveforms are extracted using fast Fourier transform (FFT) and compared against the proposed analytical models. The analytical model is in excellent agreement with the simulation results. From (23), for $M_0 = 0.8$ the term $\sin((mM_0 + n)\frac{\pi}{2})$ is non-zero for all $n = 0, \pm1, \pm2, \pm3\ldots$, this is also depicted in SM voltage harmonic spectrum in Fig. 9(a). From arm voltages (24), for $M_0 = 0.8$ and $N\ M_0 = 4$ the term $\sin((mNM_0 + n)\frac{\pi}{2})$ is nonzero for $n = \pm1, \pm3\ldots$ as shown in Fig. 9(b). The harmonics of the order $n = \pm1, \pm3\ldots$ at $m = 1$ are eliminated from the output voltage [see Fig. 9(d)] by choosing $\theta_p = \frac{\pi}{2N} = 18^{\rm o}$ (31) thus making the term $\sin(\frac{n\pi+2mN\theta_p}{2})$ zero in (26). This way, the effective switching frequency is moved to $4Nf_c$ ($m = 2$).

The time-domain waveforms and the extracted harmonic spectrum for $M_1 = 1.05$, $M_0 = 0.75$ $(= 3/4)$ are shown in Fig. 10. For $M_0 = 0.75$ and $N\ M_0 = 3.75$ the term $\sin((mNM_0 + n)\frac{\pi}{2})$ is nonzero for $n = 0, \pm1, \pm2, \pm3\ldots$ as seen in the arm voltage harmonic spectrum in Fig. 10(b). The amplitude of the harmonics in the arm voltage is higher for $n = \pm1, \pm3\ldots$ as compared to the harmonics for $n = \pm0, \pm2\ldots$. With round $(NM_0) =$ even, the optimal angle is $\theta_p = 18^{\rm o}$ (31) depicted by the lower amplitude of harmonics in Fig. 10(d) as compared to Fig. 10(c). Here, $\theta_p = 0^{\rm o}$ eliminates harmonics of the order $n = \pm0, \pm2\ldots$ and $\theta_p = 18^{\rm o}$ eliminates harmonics of the order $n = \pm1, \pm3\ldots$ at $m = 1$ from the output voltage (26). The effective switching frequency of the output voltage is $2Nf_c$ but the harmonic amplitudes are lower with $\theta_p = 18^{\rm o}$ (31).

The time-domain waveforms and the extracted harmonic spectrum for $M_1 = 1.2$, $M_0 = 0.6$ $(= 3/5)$ are shown in Fig. 11. For $M_0 = 0.6$ and $N\ M_0 =$ odd the term $\sin((mNM_0 + n)\frac{\pi}{2})$ is non zero for $m = 1$ and $n = 0, \pm2, \ldots$ as seen in the arm voltage harmonic spectrum in Fig. 11(b). The harmonics of the order $n = 0, \pm2\ldots$ at $m = 1$ are eliminated from the output voltage [see Fig. 11(c)] by choosing $\theta_p = 0$ (31) thus making the term $\sin(\frac{n\pi+2mN\theta_p}{2})$ zero in (26). Here, the effective switching frequency of the output voltage is $4\ Nf_c$ with $\theta_p = 0^{\rm o}$ (31).

As explained earlier, the best design scenario for FB-MMC is selection of $M_0 = K/N$ where $K = 1, 2, 3\ldots$ along with optimal θ_p (31). This way, the effective switching frequency at output voltage is moved to $4Nf_c$ (see Figs. 9 and 11). However, for systems where $M_0 \neq K/N$ (see Fig. 10), the harmonics are still minimized with θ_p (31) but the effective switching frequency of the output voltage is $2Nf_c$.

B. Number of Voltage Levels

It is clear from Figs. 9–11, that the number of voltage levels in the output voltage is higher for optimal θ_p given by (31). Therefore, not only the THD is lower with reduced filter size but also the *dv/dt* on the ac side components is lower with the chosen θ_p (31). In general, the number of voltage levels in the arm voltage is $((N + F) + 1)$ which are increased to $(2(N + F) + 1)$ at the output voltage with optimal θ_p (31).

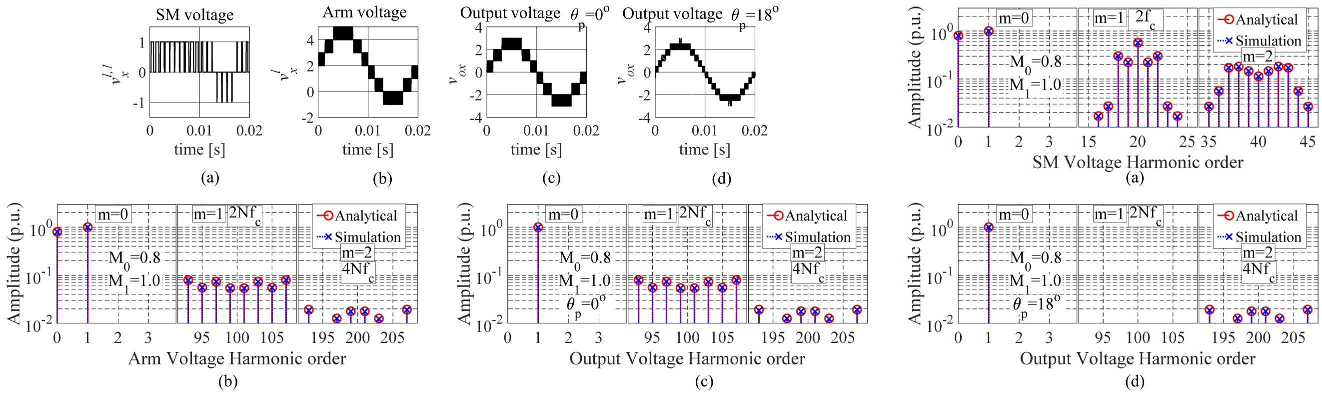

Fig. 9. Time domain waveforms and harmonic spectrum at $M_0 = 0.8\ (= 4/5)$, $M_1 = 1.0$, $N = 5$, $f_o = 50$ Hz, $f_c = 500$ Hz. N x $M_0 =$ even. (a) SM voltage. (b) Arm voltage. (c) Output voltage for $\theta_p = 0^{\circ}$. (d) Output voltage for $\theta_p = 18^{\circ}$

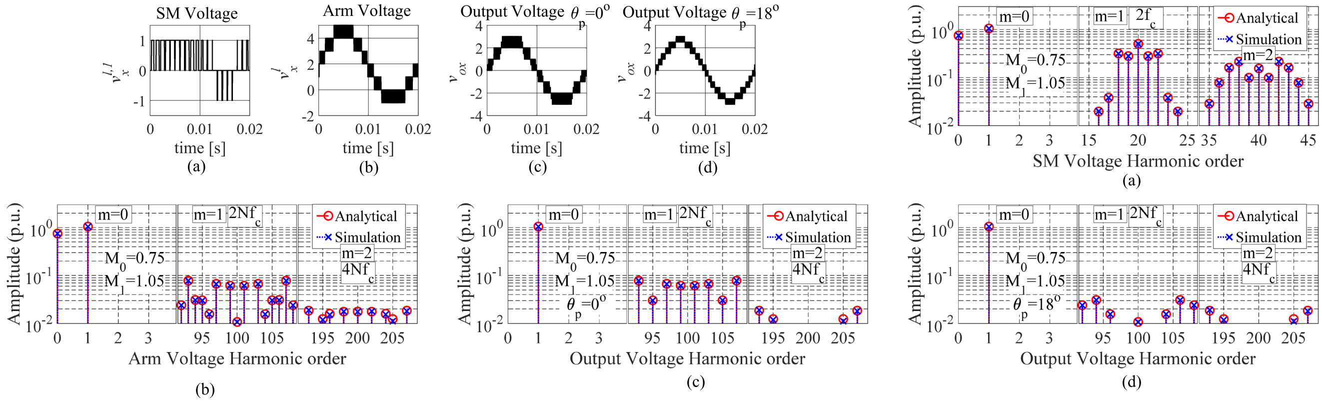

Fig. 10. Time domain waveforms and harmonic spectrum at $M_0 = 0.75\,(= 3/4)$, $M_1 = 21/20$, $N = 5$, $f_o = 50\,$Hz, $f_c = 500\,$Hz. N x $M_0 = 3.75$, nearest integer is odd. (a) SM voltage. (b) Arm voltage. (c) Output voltage for $\theta_p = 0^{\circ}$. (d) Output voltage for $\theta_p = 18^{\circ}$.

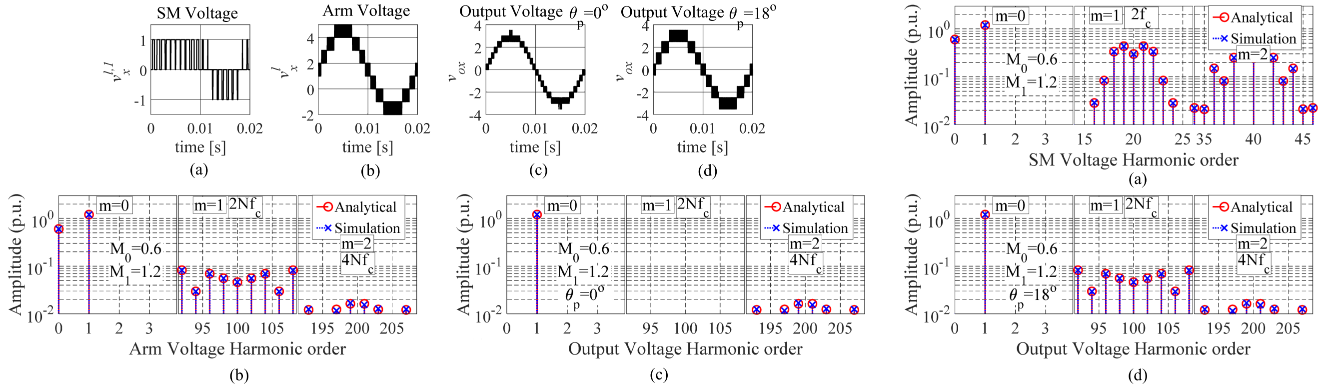

Fig. 11. Time domain waveforms and harmonic spectrum at $M_0 = 0.6\ (= 3/5)$, $M_1 = 6/5$, $N = 5$, $f_o = 50$ Hz, $f_c = 500$ Hz. N x $M_0 =$ odd. (a) SM voltage. (b) Arm voltage. (c) Output voltagege for $\theta_p = 0^{\circ}$.(d) Output voltagege for $\theta_p = 18^{\circ}$.

Here, F is the total number of (discrete) negative-voltage levels and is given by (from Fig. 3)

$$F = \text{ceil}\left\{\left(V_m - \frac{E}{2}\right)/V_c^0\right\}. \tag{33a}$$

Further, using (16) and simplifying we get

$$F = \text{ceil}\left\{\frac{N\,(M_1 - M_0)}{2}\right\}. \tag{33b}$$

Using (33), we get $F = 1$ for $M_0 = 0.8$, $M_1 = 1.0$ and for $M_0 = 0.75$, $M_1 = 1.05$ whereas $F = 2$ for $M_0 = 0.6$,

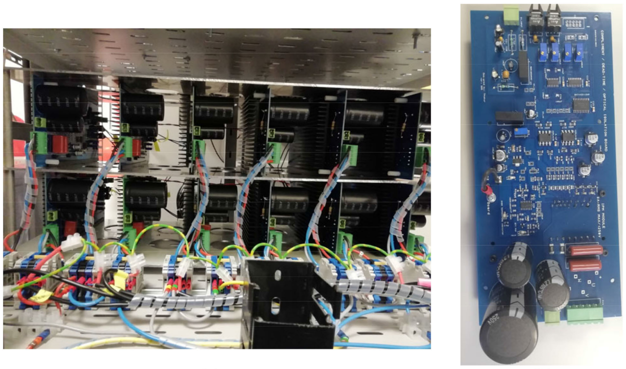
(a) (b)

Fig. 12. Three-phase experimental MMC prototype. (a) Three-phase MMC. (b) Submodule.

TABLE I
PARAMETERS OF MMC EXPERIMENTAL PROTOTYPE

AC frequency	50Hz
Load peak current	6.8A
Load resistance	10Ω
AC impedance (R_g, L_g)	0.25Ω, 1.85mH
DC-link voltage (E)	61.5, 128V
Average SM capacitor voltage (V_c^0)	46.5, 76.5V
Modulation index ratio M_1/M_0	1/0.8, 1.3/0.5
Number of submodules of each arm (N)	2
Arm impedance (R_b, L_b)	0.12Ω, 1.85mH
Module capacitance (C)	0.66mF
Switching frequency	2500Hz

$M_1 = 1.2$. Therefore, the number of voltage levels (including the zero state) in arm voltage is 7, 7, and 8 for the three cases as depicted in Figs. 9–11, respectively. The number of levels in the output voltage increases to 13 [see Fig. 9(d)], 13 [see Fig. 10(d)] and 15 [see Fig. 11(c)] with optimal θ_p.

VII. EXPERIMENTAL VALIDATION

The analytical model is validated against the experimental results. A three-phase FB-MMC prototype with $N = 2$ (see Fig. 12) is used in this article. The intelligent power module IKCM20L60GDXKMA1 from INFINEON is used to design each FBSM and OPAL-RT 5607 is the control platform. The dc side of MMC is fed by a dc power supply and the ac side is connected to passive load of 10Ω. The experimental setup parameters are given in Table. I. The harmonic distribution is calculated by applying FFT to the captured PWM voltage waveforms which are sampled at 2us. The experiment is performed for two different cases of boost mode: (e1) $M_0 = 0.8\,(= 4/5)$, $M_1 = 1$, $V_c^0 = 76.5$ V, $E = 128\,$V, and (e2) $M_0 = 0.5$ $(= 1/2)$, $M_1 = 1.3$, $V_c^0 = 46.5$ V, $E = 61.5$V.

The FB-MMC is operated in circulating current suppressed mode, i.e., the circulating currents are actively suppressed to zero by dedicated PI controllers in second harmonic reference frame [49]. The individual balancing is achieved by dedicated proportional controllers which add a small duty ratio in relation to the direction of arm current [16]. The modulation signal parameters M_0 and M_1 are fed directly to the control and the dc voltage is controlled to maintain same load current i.e., load voltage. In other words, the boost operation is obtained by reduced dc voltage for fixed ac/load voltage. The control block diagram is shown in Fig. 13.

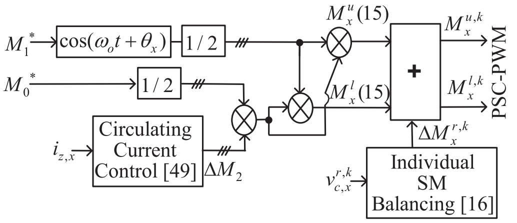

Fig. 13. Control block diagram used in experiment.

The steady-state scope results are shown in Figs. 14 and 15 for the two cases. As expected for the boost mode, the negative-voltage states of FBSMs are utilized as seen in the SM and the arm voltages. The FFT results of the measured output voltage are compared to the analytical harmonic spectra in Figs. 14 and 15 for the two angles $\theta_p = 0^o$ and $\theta_p = 45^o$ $(= \pi/2N)$. The analytical model closely matches the experimetal results. The minor discrepancies can be noticed at $m = 1$ [see Fig. 15(a)] where small harmonic amplitudes appear, mainly due to the effect of the SM capacitor votlage ripple and circulating current control [50]. For case (e1) complete harmonic elimination is not achieved at $m = 1$ (harmonic order of 200) for either $\theta_p = 0$ or $\theta_p = 45^o$ as shown in Fig. 14(a) and (b). This is expected as N x $M_0 =$ fraction. The rms values of harmonics at $m = 1$ for case(e1) are calculated as $v_{ox}^{\{1,n\}} = 0.313$ at $\theta_p = 0$ and $v_{ox}^{\{1,n\}} = 0.274$ at $\theta_p = 45^o$.Therefore, the harmonic minimization for case(e1) is achieved at $\theta_p = 45^o$ which is justified as round $(N$ x $M_0) =$ even as given by (31).

Complete harmonic elimination at $m = 1$ in the output voltage is achieved for cases (e2) with N x $M_0 =$ odd [see Fig. 15(a)]. The harmoncis at $m = 1$ are eliminated in the output voltage (26) [see Fig. 15(a)] by choosing $\theta_p = 0^o$ (31), thus shifting the effective switching frequency to $4Nf_c$, i.e., harmonic order of 400. The experimental results verify both the accuracy of the analytical harmonic model (26) and the proposed optimal interarm PSC angle (31).

The number of voltages levels in the output voltage v_{ox} is higher for optimal angle i.e., (e1) $\theta_p = 45^o$ for $M_0 = 0.8$ and N $= 2$ and (e2) $\theta_p = 0^o$ for $M_0 = 0.5$ and $N = 2$ as defined by (31). The observed number of voltage levels in both cases is 7 (i.e., $(2(N+F)+1)$, $N = 2$, $F = 1$, (33)) as seen in Figs. 14(b) and 15(a). It is clear that for best harmonic optimization and for higher effective switching frequency of $4Nf_c$ the product N x M_0 should be designed as (or close to) an integer, i.e., $M_0 = K/N$ where $K = 1, 2, 3\ldots$ which in this case is for $N = 2$ and $M_0 = 0.5 (= 1/2)$. Also, the number of voltage levels is increased with the proposed θ_p (31) thereby reducing the *dv/dt* seen by the ac side components.

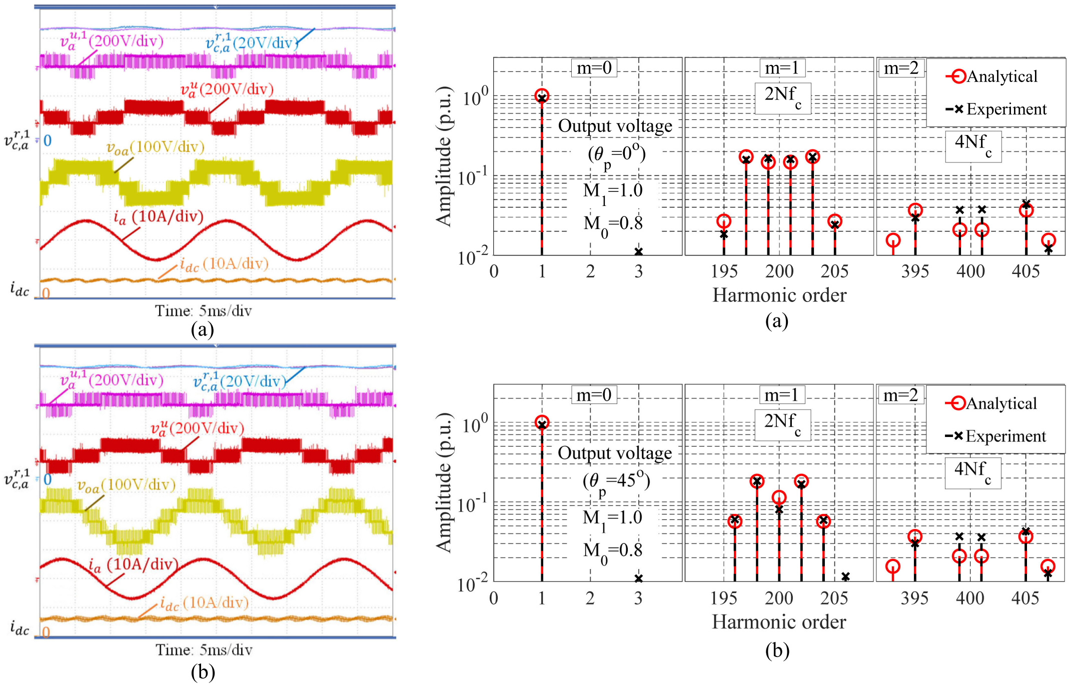

Fig. 14. Steady-state time domain experimental results and harmonic spectrum of measured output voltage. Case (e1) $M_0 = 0.8\ (= 4/5)$, $M_1 = 1$, $V_c^0 = 76.5\,\text{V}$, $E = 128\,\text{V}$. (a) $\theta_p = 0°$. (b) $\theta_p = 45°$.

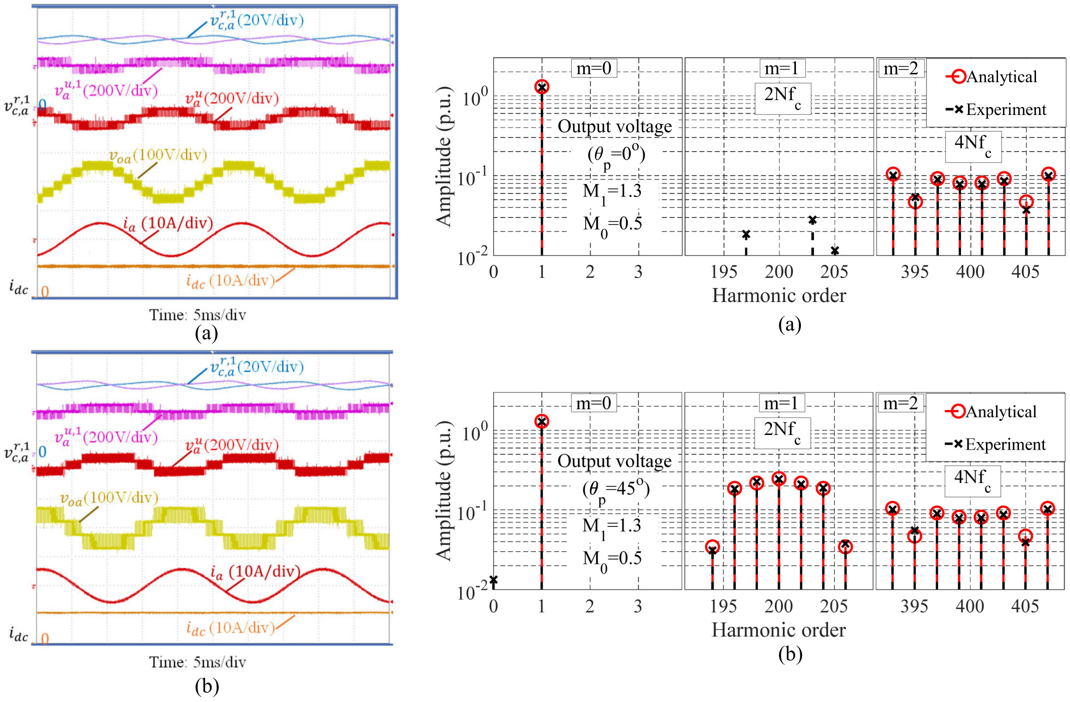

Fig. 15. Steady-state time domain experimental results and harmonic spectrum of measured output voltage. Case (e2) $M_0 = 0.5\ (= 1/2)$, $M_1 = 1.3$, $V_c^0 = 46.5\text{V}$, $E = 61.5\text{V}$. (a) $\theta_p = 0°$. (b) $\theta_p = 45°$.

TABLE II
COMPARISON BETWEEN CONVENTIONAL (BUCK) AND BOOSTED MODULATION FB-MMC

	FB-MMC-1 (Buck)	FB-MMC-2 (Boost)
$V_{l\text{-}l}$ (rms line-to-line)	3.3 kV	3.3 kV
AC side power	5MW	5MW
E	6.0 kV	3.85 kV
L_{gn}	0.69 mH	0.69 mH
k_m	0.9	1.4
M_1/M_0	0.9/1.0	1.05/0.75
V_c^0	1.5 kV	1.285 kV (-14.3%)
N	4	4
C	22.7 mF	22.7 mF
ΔV_c	4.1%	2.2% (- 46%)
$I_{arm,rms}$	518 A	614 A (+ 18%)
f_o , f_c	50Hz, 500Hz	50Hz, 500Hz
Circulating current control	Yes	Yes
Existing [40] Optimized for buck mode operation	$\theta_p = 22.5^o$ THD = 16.73%	$\theta_p = 22.5^o$ THD = 28.46%
Proposed (31) Optimized for buck-boost mode operation	$\theta_p = 22.5^o$ THD = 16.73%	$\theta_p = 0^o$ THD = 13.24%

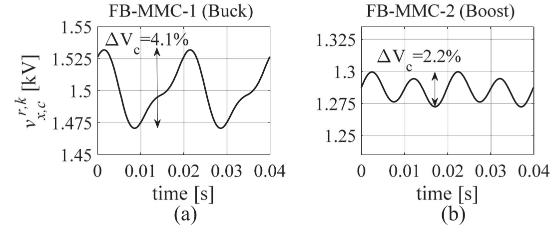

Fig. 16. Simulations results of SM capacitor voltages in (a) FB-MMC-1 (buck) and (b) FB-MMC-2 (boost).

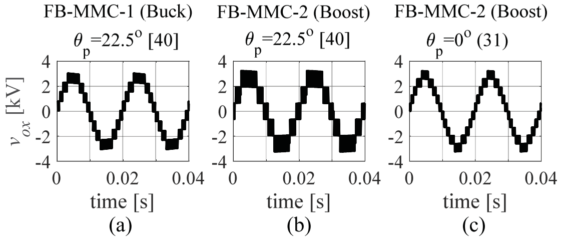

Fig. 17. Simulation results of output voltages (a) FB-MMC-1, $\theta_p = \pi/2N(=22.5^o)$ optimized for buck mode [40]. (b) FB-MMC-2, $\theta_p = 22.5^o$ optimized for buck mode [40]. (c) FB-MMC-2, $\theta_p = 0^o$ optimized for boost mode (31).

VIII. DISCUSSION

A. Comparison With the Existing Method and Benefits of Boost Mode

It is well established in the literature that the operation of FB-MMC in boost mode at the optimal input/output voltage ratio i.e., modulation index [17], [19] benefits from improved device utilization and lower SM capacitor voltage ripple. This article further improves the FB-MMC operation in boost mode by optimising the output voltage harmonic spectrum. For the sake of completeness, a comparative study including both buck and boost modes of operation is presented in this section. The parameters of the MMC considered in this simulation study are given in Table II. The comparison is made between FB-MMC-1 which is the conventional design operating in the buck mode (with modulation index of 0.9) and FB-MMC-2 which is operated in boost mode. At the same time the comparison is made with the existing PSC-PWM approach [40] developed for the conventional buck mode. The system details are given in Table. II. In this article, the number of SMs and ac side voltage and power are set to be fixed, based on which the FB-MMC-1 is designed. The FB-MMC-2 is operated in the boost mode by reducing the dc side voltage to achieve the optimal modulation index of 1.4 (at which energy variations and SM capacitor voltage ripple are at a minimum). The FB-MMC-2 has increased rms current, reduced voltage stress and greatly reduced SM capacitor voltage ripple ($\sim$ (-46%), Table II). The steady-state time domain SM capacitor voltages are shown in Fig. 16 clearly depicting the reduced SM capacitor voltage ripple in FB-MMC-2 (for the same SM capacitance). The time-domain output voltages are shown in Fig. 17 and the harmonic spectrum (obtained by applying FFT on the switching waveforms) is shown in Fig. 18.

The existing analytical model proposed in [40] is given in Appendix B. From (B2) [40], the optimal angle in the buck mode is $\theta_p = 22.5^o$ for $N = 4$. From Fig. 18(a) it can be seen that the complete harmonic elimination at $m = 1$ is achieved in FB-MMC-1 (and analytical solution (B1) [40] matches the simulation results). However, if the $\theta_p = 22.5^o$ (optimized for buck mode [40]) is used in boost mode operation (FB-MMC-2), harmonic elimination is not achieved at $m = 1$ (and analytical solution (B1) [40] does not match the simulation results). On the other hand, with the proposed optimum angle of $\theta_p = 0^o$ [expression (31) for $N = 4$ and $M_o = 3/4$] complete harmonic cancellation at $m = 1$ is also achieved in FB-MMC-2 [and analytical solution (26) matches the simulation results]. Therefore, by applying the optimisation approach proposed in this article the first dominate sideband harmonics appear at frequency of $4Nf_c$ for both buck and boost modes, which greatly simplifies the output filter design. Of note, the PSC-PWM analysis in [40] is proposed for FB-MMC operation in the buck mode ($M_0 = 1$) and is sufficient for that mode of operation. In fact, the analytical solution proposed in this article is generic, in that it is applicable to both buck and boost modes of operation with expressions (26) and (31) converging, respectively, into (B1) and (B2) [40] for $M_0 = 1$ (buck mode).

B. Effect of Increased SM Capacitor Voltage Ripple on the Harmonic Spectrum

This simulation study is based on the MMC parameters given in Table II. In this article, the SM capacitor voltage ripple is considered to be small and negligible (ΔV_c< 5%, Table II) and SM capacitor voltage is assumed to be pure dc for simplicity

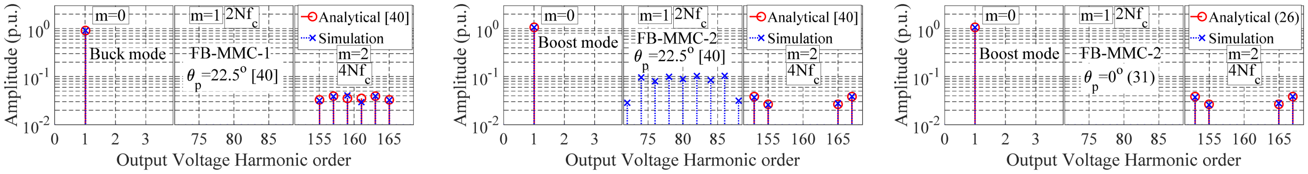

(a) (b) (c)

Fig. 18. Harmonic spectrum of (a) FB-MMC-1 with $\theta_p = \pi/2N (= 22.5^\circ)$ optimized for buck mode [40]. (b) FB-MMC-2 with $\theta_p = 22.5^\circ$ optimized for buck mode [40]. (c) FB-MMC-2 with proposed $\theta_p = 0^\circ$ optimized for boost mode (31).

TABLE III
SUMMARY OF HARMONIC COMPONENTS FROM FIGS. 19 AND 21

		FFT of modulation signal			FFT of SM capacitor voltage			
Parameter	SM capacitance	M_0	M_1	M_2	V_c^0 (V)	V_c^1 (V)	V_c^2 (V)	ΔV_c (%)
FB-MMC-1	C	1.0	0.9	0.0146	1500	25.73	9.69	4.09
	$0.2 * C$	1.0	0.9	0.0707	1500	128.54	48.5	20.47
FB-MMC-2	C	0.75	0.75	0.0067	1285	3.29	11.33	2.12
	$0.2 * C$	1.05	1.05	0.0343	1285	16.88	56.93	10.65

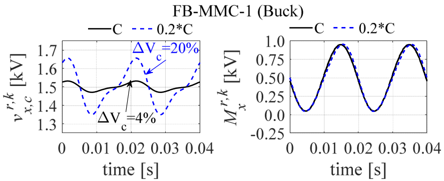

(a) (b)

Fig. 19. Buck mode operation (FB-MMC-1) with C and $0.2 * C$. (a) SM capacitor voltages. (b) modulation signal.

[40]. For the sake of completeness, in this section the simulation results and analysis are provided for FB-MMC operation (in both buck and boost modes) with considerable SM capacitor voltage ripple (above 10%) by reducing the SM capacitance to 20% of C (where C is given in Table II).

The time domain waveforms of SM capacitor voltage and the modulation signal for FB-MMC-1 operating in the buck mode are presented in Fig. 19 (as given in Table II) clearly showing an increase in SM capacitor voltage ripple ΔV_c from 4% to 20% by decreasing the SM capacitance from C to $0.2 * C$. The major harmonics of the modulation signal and SM capacitor voltage shown in Fig. 19 are given in Table III in Appendix C. It can be seen in Fig. 20 that the output voltage harmonic spectrum is optimal at $\theta_p = 22.5^\circ$ as given by (31) for both values of SM capacitance (i.e., C and $0.2 * C$). Notice that even with $\Delta\ V_c = 20\%$ the harmonics which are not eliminated at $m = 1$ are $< 3\%$ i.e., very low.

The time domain waveforms of the FB-MMC-2 operating in boost mode are shown in Fig. 21. As expected, at the optimal modulation index of $k_m = 1.41$ the ΔV_c is reduced to 10% compared to the operation in the buck mode with $\Delta\ V_c = 20\%$ for the same SM capacitance (see Fig. 19). The major harmonics of the modulation signal and SM capacitor voltage shown in Fig. 21 are given in Table III in Appendix C. The output voltage harmonic spectrum is shown in Fig. 22 with the optimal angle of $\theta_p = 0$ as given by (31). The harmonics that appear at $m = 1$ in Fig. 22(a) are reduced ($<2\%$) compared to the harmonics at $m = 1$ in the buck mode [see Fig. 20(b)] due to operation at the optimum input/output voltage ratio. It is clear from Figs. 20 and 22 that the increase in SM capacitor voltage ripple introduces additional harmonics in the output voltage harmonic spectrum at $m = 1$, however, the optimisation method of the output voltage harmonic spectrum proposed in this article does not change with the change in SM capacitor voltage ripple and is still given by proposed expression (31).

The analytical solution of the output voltage harmonic spectrum of FB-MMC considering the SM capacitor voltage ripple does not exist in the literature. However, the analytical origin and analysis of the additional harmonics at $m = 1$ for HB-MMC are previously demonstrated in [50]. The SM capacitor voltage ripple affects the harmonic spectrum in two ways: first, the SM capacitor voltage harmonics interact with the modulation signal introducing additional harmonics [50], and second, the SM capacitor voltage ripple introduces dominant second-order circulating currents which require compensation in the form of the second-order modulation signal [51]. The introduced second order modulation signal also affects the output voltage harmonic spectrum as was demonstrated in [50].

Under normal operating conditions, the SM capacitance is designed to limit the capacitor voltage ripple within $\pm 10\%$ [40] (i.e., $\Delta V_c < 20\%$) and for these conditions the effect of the SM capacitor voltage ripple can be neglected as demonstrated in Figs. 20 and 22 where the introduced harmonics are $<3\%$. However, for converters operating with high SM capacitor voltage ripple ($\Delta V_c > 20\%$), the voltage ripple might significantly affect the output filter design. The analytical modelling and analysis of low-capacitance FB-MMC (with $\Delta V_c > 20\%$) is beyond the scope of this article and will be investigated in the future.

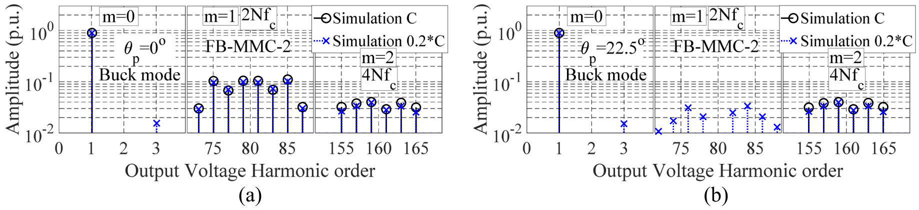

(a) (b)

Fig. 20. Buck mode operation (FB-MMC-1) output voltage harmonic spectrum with C and $0.2 * C$. (a) With $\theta_p = 0$. (b) With proposed $\theta_p = \pi/2N (= 22.5^{\circ})$ (31).

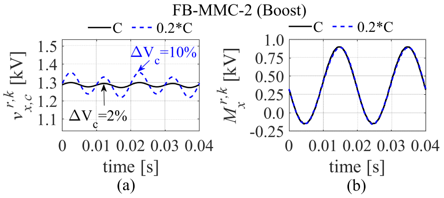

(a) (b)

Fig. 21. Boost mode operation (FB-MMC-2) with C and $0.2 * C$. (a) SM capacitor voltages. (b) Modulation signal.

IX. CONCLUSION

The conventional modulation signal of PSC-PWM is extended for FB-MMC operation in boost mode, i.e., where boosted ac voltage is obtained by utilizing the FBSM negative-voltage states. The modulation signal comprises a fundamental modulation component M_1 and a dc component M_0. The analytical output voltage harmonic spectrum of the FB-MMC operating in boost mode is developed and the additional harmonic sidebands are clearly identified. Although the magnitude of the harmonics is affected by the fundamental modulation amplitude M_1, the order of the harmonics itself is mainly defined by the number of SMs N and the dc modulation component M_0. For output voltage harmonic minimization with a given number of SMs N, the dc modulation component should be chosen as $M_0 = K/N$ where $K = 1, 2, 3 \ldots$ or in general the product N x M_0 should be designed to be an integer. Having $M_0 = K/N$ and the proposed optimal upper/lower arm carrier phase angle θ_p, the first group of harmonics centered at $2Nf_c$ are eliminated thereby shifting the effective switching frequency i.e., first group of nonzero harmonics to $4Nf_c$ in the output voltage. This way, the filter cut-off frequency is doubled greatly reducing filter size. At the same time, the number of voltage levels is higher with the proposed θ_p thereby reducing the dv/dt voltage stress on the ac side components.

For systems where $M_0 \neq K/N$, the effective switching frequency of the output voltage stays at $2Nf_c$. However, with the proposed optimal θ_p partial harmonic elimination is achieved thereby reducing the rms of the harmonics. This way, the filter size could still be reduced.

The energy storage requirement in the FB-MMC is reduced in boost mode by choosing the appropriate modulation index (dc to ac voltage ratio) i.e., the ratio of modulation index parameters M_1 and M_0. At the same time by optimally selecting the number of SMs N and the inter arm carrier phase shift angle θ_p the harmonics at the output voltage can be greatly minimized.

APPENDIX A

General Form: The harmonic spectrum of a general carrier-based PWM waveform can be expressed by

$$f\ (t) = \frac{C_{00}}{2} + Re \sum_{n\,=\,1}^{\infty} C_{0,n} e^{-jny}$$

$$+ Re \sum_{m\,=\,1}^{\infty} \sum_{n\,=\,-\infty}^{n\,=\,\infty} C_{m,n} e^{-j(mz+ny)} \tag{A0a}$$

where the coefficients are defined as

$$C_{m,n} = \frac{1}{2\pi^2} \int_{-\pi}^{\pi} \int_{-\pi}^{\pi} f\ (z, y)\, e^{j(mz+ny)} dz\ dy. \tag{A0b}$$

Here, Re indicates the real part of the complex quantity.

Derivation of (23): Using the LL and RL voltages given by (22), the SM output voltage in the lower arm is given by

$$v_x^{l,k} = v_{x,LN}^{r,k} - v_{x,RN}^{r,k} \tag{A1}$$

$$= V_c^0 \left(\frac{M_0}{2}\right) + \frac{V_c^0 M_1}{2} \cos(y) + \mathrm{Re} \sum_{m\,=\,1}^{\infty} \sum_{n=-\infty}^{\infty} e^{-j(ny+mz)}$$

$$\times \left[\frac{2V_c^0}{m\pi} J_n \left(mM_1 \frac{\pi}{4}\right) \left\{\sin\left(\left(m\left(1+\frac{M_0}{2}\right)+n\right)\frac{\pi}{2}\right)\right.\right.$$

$$\left.\left.-(-1)^n \sin\left(\left(m\left(1-\frac{M_0}{2}\right)+\mathrm{n}\right)\frac{\pi}{2}\right)\right\}\right].$$

Rewriting (A1) by expanding the sine and cosine terms we get

$$v_x^{l,k} = V_c^0 \left(\frac{M_0}{2}\right) + \frac{V_c^0 M_1}{2} \cos(y)$$

$$+ \mathrm{Re} \sum_{m\,=\,1}^{\infty} \sum_{n\,=\,-\infty}^{\infty} e^{-j(ny+mz)} \tag{A2}$$

$$\times \left[\frac{2V_c^0}{m\pi} J_n \left(mM_1 \frac{\pi}{4}\right)\right]$$

$$\times \left[\begin{array}{c} \left\{(1-(-1)^n) \sin\left((m+n)\frac{\pi}{2}\right) \cos\left(\frac{mM_0\pi}{4}\right)\right\} \\ +\left\{(1+(-1)^n) cos\left((m+n)\frac{\pi}{2}\right) \sin\left(\frac{mM_0\pi}{4}\right)\right\} \end{array}\right].$$

For m is odd, $v_x^{l,k}$ is zero. Therefore m is replaced by $2m$ in (A2) and we get

$$v_x^{l,k} = V_c^0 \left(\frac{M_0}{2}\right) + \frac{V_c^0 M_1}{2} \cos(y)$$

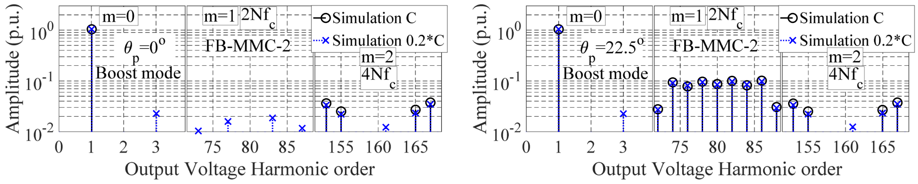

(a) (b)

Fig. 22. Boost mode operation (FB-MMC-2) output voltage harmonic spectrum with C and $0.2 * C$. (a) With proposed $\theta_p = 0$ (31). (b) With $\theta_p = \pi/2N(= 22.5^{\mathrm{o}}$).

$$+ \mathrm{Re} \sum_{m\,=\,1}^{\infty} \sum_{n\,=\,-\infty}^{\infty} e^{-j(ny+2mz)} \tag{A3a}$$

$$\times \left[\frac{V_c^0}{m\pi} J_n \left(m M_1 \frac{\pi}{2} \right) \right]$$

$$\times \left[\begin{array}{l} \left\{ \left(1-(-1)^n\right) \sin\left((2m+n)\frac{\pi}{2}\right) \cos\left(\frac{mM_0\pi}{2}\right) \right\} \\ - \left\{ \left(1+(-1)^n\right) \cos\left((2m+n)\frac{\pi}{2}\right) \sin\left(\frac{mM_0\pi}{2}\right) \right\} \end{array} \right].$$

Further rewriting (A3) as

$$v_x^{l,k} = V_c^0 \left(\frac{M_0}{2} \right) + \frac{V_c^0 M_1}{2} \cos(y) \tag{A3b}$$

$$+ \mathrm{Re} \sum_{m\,=\,1}^{\infty} \sum_{n\,=\,-\infty}^{\infty} e^{-j(ny+2mz)}$$

$$x \left[\frac{V_c^0}{m\pi} J_n \left(m M_1 \frac{\pi}{2} \right) \right]$$

$$\times \left[\begin{array}{l} \quad \left\{ \left(1-(-1)^n\right) \sin\left(\frac{n\pi}{2}\right) \cos(m\pi) \cos\left(\frac{mM_0\pi}{2}\right) \right\} \\ + \left\{ \left(1+(-1)^n\right) \cos\left(\frac{n\pi}{2}\right) \cos(m\pi) \sin\left(\frac{mM_0\pi}{2}\right) \right\} \end{array} \right].$$

In (A3) the term $(1-(-1)^n)\sin(\frac{n\pi}{2})$ is nonzero for n is odd and is, replaced with $2\sin(\frac{n\pi}{2})$. Similarly, the term $(1+(-1)^n)\cos(\frac{n\pi}{2})$ is nonzero for n is even and is replaced with $2\cos(\frac{n\pi}{2})$. Further simplification leads to lower arm SM output voltage (23a).

Derivation of (24a): the (lower) arm voltage is given by

$$v_x^l = \sum_{k=1}^{N} v_x^{l,k} = \frac{N M_0 V_c^0}{2} + \frac{N M_1 V_c^0}{2} \cos(\omega_o t + \theta_x) \tag{A4}$$

$$+ \mathrm{Re} \sum_{m\,=\,1}^{\infty} \sum_{n\,=\,-\infty}^{\infty} \left(\sum_{k\,=\,1}^{N} e^{-j\left(n(\omega_o t+\theta_x)+2m\left(\omega_c t+\frac{\pi}{N}(k-1)\right)\right)} \right)$$

$$\times \left[\frac{2V_c^0}{m\pi} J_n \left(m M_1 \frac{\pi}{2} \right) \cos(m\pi) \sin\left((mM_0+n) \frac{\pi}{2} \right) \right]$$

where

$$\sum_{k\,=\,1}^{N} e^{-j\left(n(\omega_o t+\theta_x)+2m\left(\omega_c t+\frac{\pi}{N}(k-1)\right)\right)} \tag{A5}$$

$$= \left\{ \begin{array}{r} 0 \text{ for } m \neq KN,\ K=1,\ 2,\ 3\ldots, \\ N e^{-j(n(\omega_o t+\theta_x)+2m(\omega_c t))} \text{ for } m = KN,\ K=1,\ 2,\ 3\ldots, \end{array} \right. .$$

Using (A5) in (A4) and further simplifying by replacing $m \to Nm$ we get (24a). Similarly upper arm voltage (24b) is derived.

Appendix B

Existing PSC-PWM approach in [40] proposed for the buck mode of operation [$M_0 = 1$ in (15)] is briefly introduced here. The output voltage harmonic spectrum is given by

$$v_{ox} = \frac{N M_1 V_c^0}{2} \cos(\omega_o t + \theta_x) \tag{B1}$$

$$+ \sum_{m\,=\,1}^{\infty} \sum_{n\,=\,-\infty}^{\infty}$$

$$\mathrm{Sin} \left((n(\omega_o t + \theta_x) + 2mN\omega_c t) + \frac{(n\pi + 2mN\theta_{psc})}{2} \right)$$

$$\times \left[\frac{2V_c^0}{m\pi} J_n \left(mNM_1 \frac{\pi}{2} \right) \cos(mN\pi) \sin\left((mN+n) \frac{\pi}{2} \right) \right]$$

$$\times \left[\sin\left(\frac{n\pi + 2mN\theta_{psc}}{2} \right) \right]$$

Based on (B1), the optimal inter-arm phase shift angle that eliminates harmonics at $m = 1$ (thereby shifting effective switching frequency to $4Nf_c$) is given by

$$\theta_p = 0, \{N \text{ is odd} \tag{B2}$$

$$\theta_p = \frac{\pi}{2N}, \{N \text{ is even}.$$

Appendix C

The individual harmonic components in the SM capacitor voltages (V_c^i, $i = 0, 1, 2$) and the modulation signal (M_i, $i = 0, 1, 2$) are extracted from the time domain simulations (see Figs. 19 and 21) and given in Table III to demonstrate the relative increase in voltage ripple and M_2 at $0.2 * C$.

Acknowledgment

The authors would like to thank the engineers of Siemens Gamesa Renewable Energy, Sheffield, U.K., for their valuable feedback.

References

[1] S. Debnath, J. Qin, B. Bahrani, M. Saeedifard, and P. Barbosa, "Operation, control, and applications of the modular multilevel converter: A review," *IEEE Trans. Power Electron.*, vol. 30, no. 1, pp. 37–53, Jan. 2015.

[2] H. Akagi, "Classification, terminology, and application of the modular multilevel cascade converter (MMCC)," *IEEE Trans. Power Electron.*, vol. 26, no. 11, pp. 3119–3130, Dec. 2011.

[3] H. Akagi, "A review of developments in the family of modular multilevel cascade converters," *IEEJ Trans. Elect. Electron. Eng.*, vol. 13, no. 9, pp. 1222–1235, Sep. 2018.

[4] A. Nami, J. Liang, F. Dijkhuizen, and G. D. Demetriades, "Modular multilevel converters for HVDC applications: Review on converter cells and functionalities," *IEEE Trans. Power Electron.*, vol. 30, no. 1, pp. 18–36, Jan. 2015.

[5] M. A. Perez, S. Bernet, J. Rodriguez, S. Kouro, and R. Lizana, "Circuit topologies, modeling, control schemes, and applications of modular multilevel converters," *IEEE Trans. Power Electron.*, vol. 30, no. 1, pp. 4–17, Jan. 2015.

[6] S. Kouro *et al.*, "Recent advances and industrial applications of multilevel converters," *IEEE Trans. Ind. Electron.*, vol. 57, no. 8, pp. 2553–2580, Aug. 2010.

[7] M. Malinowski, K. Gopakumar, J. Rodriguez, and M. A. Perez, "A survey on cascaded multilevel inverters," *IEEE Trans. Ind. Electron.*, vol. 57, no. 7, pp. 2197–2206, Jul. 2010.

[8] K. Ilves, S. Member, A. Antonopoulos, S. Member, and S. Norrga, "Steady-state analysis of interaction between harmonic components of arm and line quantities of MMC," *IEEE Trans. Power Electron.*, vol. 27, no. 1, pp. 57–68, Jan. 2012.

[9] Q. Song, W. Liu, X. Li, H. Rao, S. Xu, and L. Li, "A steady-state analysis method for a modular multilevel converter," *IEEE Trans. Power Electron.*, vol. 28, no. 8, pp. 3702–3713, Aug. 2013.

[10] R. Oliveira and A. Yazdani, "An enhanced steady-state model and capacitor sizing method for modular multilevel converters for HVdc applications," *IEEE Trans. Power Electron.*, vol. 33, no. 6, pp. 4756–4771, Jun. 2018.

[11] K. Ilves, L. Harnefors, S. Norrga, and H. Nee, "Analysis and operation of modular multilevel converters with phase-shifted carrier PWM," *IEEE Trans. Power Electron.*, vol. 30, no. 1, pp. 268–283, Jan. 2015.

[12] N. Thitichaiworakorn, M. Hagiwara, and H. Akagi, "Experimental verification of a modular multilevel cascade inverter based on double-star bridge-cells (MMCI-DSBC)," in *Proc. IEEE Energy Convers. Congr. Expo.*, 2012, pp. 4196–4202.

[13] G. P. Adam, "Improved control strategy of full-bridge modular multilevel converter," in *Proc. IEEE Elect. Power Energy Conf.*, 2015, pp. 326–331.

[14] G. P. Adam and I. E. Davidson, "Robust and generic control of full-bridge modular multilevel converter high-voltage DC transmission systems," *IEEE Trans. Power Del.*, vol. 30, no. 6, pp. 2468–2476, Dec. 2015.

[15] J. Hu, Z. He, L. Lin, K. Xu, and Y. Qiu, "Voltage polarity reversing-based DC short circuit FRT strategy for symmetrical bipolar FBSM-MMC HVDC system," *IEEE J. Emerg. Sel. Top. Power Electron.*, vol. 6, no. 3, pp. 1008–1020, Sep. 2018.

[16] N. Thitichaiworakorn, M. Hagiwara, and H. Akagi, "Experimental verification of a modular multilevel cascaded inverter based on double-star bridge cells," *IEEE Trans. Ind. Appl.*, vol. 50, no. 1, pp. 509–519, Jan./Feb. 2014.

[17] C. Zhao, Y. Li, Z. Li, P. Wang, X. Ma, and Y. Luo, "Optimized design of full-bridge modular multilevel converter with low energy storage requirements for HVdc transmission system," *IEEE Trans. Power Electron.*, vol. 33, no. 1, pp. 97–109, Jan. 2018.

[18] G. P. Adam, S. Finney, B. Williams, I. E. Davidson, and A. Y. M. Abbas, "Full-bridge modular multilevel converter (FB-MMC) with extended control range," in *Proc. AFRICON*, 2015, pp. 1–5.

[19] Q. Song, W. Yang, B. Zhao, S. Xu, H. Rao, and Z. Zhu, "Energy storage requirement reduction using negative-voltage states of a full-bridge modular multilevel converter," *IEEE Trans. Power Electron.*, vol. 34, no. 6, pp. 5243–5255, Jun. 2019.

[20] K. Ilves, S. Norrga, and H. Nee, "On energy variations in modular multilevel converters with full-bridge submodules for ac-dc and ac-ac applications," in *Proc. 15th Eur. Conf. Power Electron. Appl.*, 2013, pp. 1–10.

[21] C. Zhao, Z. Wang, Z. Li, P. Wang, and Y. Li, "Characteristics analysis of capacitor voltage ripples and dimensioning of full-bridge MMC with zero sequence voltage injection," *IEEE J. Emerg. Sel. Topics Power Electron.*, vol. 7, no. 3, pp. 2106–2115, Sep. 2019.

[22] C. Zhao *et al.*, "Energy storage requirements optimization of full-bridge MMC with third-order harmonic voltage injection," *IEEE Trans. Power Electron.*, vol. 34, no. 12, pp. 11661–11678, Dec. 2019.

[23] J. Hu, M. Xiang, L. Lin, M. Lu, J. Zhu, and Z. He, "Improved design and control of FBSM MMC with boosted AC voltage and reduced DC capacitance," *IEEE Trans. Ind. Electron.*, vol. 65, no. 3, pp. 1919–1930, Mar. 2018.

[24] M. Xiang, J. Hu, and Y. Qiu, "Coordinated control of power loss and capacitor voltage ripple reduction for ac voltage boosted FBSM MMC with second harmonic circulating current injection," *High Voltage*, vol. 3, no. 4, pp. 272–278, 2018.

[25] R. Zeng, L. Xu, L. Yao, and B. W. Williams, "Design and operation of a hybrid modular multilevel converter," *IEEE Trans. Power Electron.*, vol. 30, no. 3, pp. 1137–1146, Mar. 2015.

[26] W. Lin, D. Jovcic, S. Nguefeu, and H. Saad, "Full-bridge MMC converter optimal design to HVDC operational requirements," *IEEE Trans. Power Del.*, vol. 31, no. 3, pp. 1342–1350, Jun. 2016.

[27] M. Lu, J. Hu, R. Zeng, W. Li, and L. Lin, "Imbalance mechanism and balanced control of capacitor voltage for a hybrid modular multilevel converter," *IEEE Trans. Power Electron.*, vol. 33, no. 7, pp. 5686–5696, Jul. 2018.

[28] L. Lin, Y. Lin, C. Xu, and Y. Chen, "Comprehensive analysis of capacitor voltage fluctuation and capacitance design for sub-modules in hybrid modular multilevel converter with boosted modulation index," *IEEE J. Emerg. Sel. Topics Power Electron.*, vol. 7, no. 4, pp. 2369–2383, Dec. 2019.

[29] P. Hu, R. Teodorescu, and J. M. Guerrero, "Negative-sequence second-order circulating current injection for hybrid MMC under over-modulation conditions," *IEEE J. Emerg. Sel. Topics Power Electron.*, vol. 8, no. 3, pp. 2508–2519, Sep. 2020.

[30] J. Lee, J. Jung, and S. Sul, "Balancing of submodule capacitor voltage of hybrid modular multilevel converter under DC-bus voltage variation of HVDC system," *IEEE Trans. Power Electron.*, vol. 34, no. 11, pp. 10458–10470, Nov. 2019.

[31] R. Darus, J. Pou, G. Konstantinou, S. Ceballos, R. Picas, and V. G. Agelidis, "A modified voltage balancing algorithm for the modular multilevel converter : Evaluation for staircase and phase-disposition PWM," *IEEE Trans. Power Electron.*, vol. 30, no. 8, pp. 4119–4127, Aug. 2015.

[32] Q. Tu and Z. Xu, "Impact of sampling frequency on harmonic distortion for modular multilevel converter," *IEEE Trans. Power Del.*, vol. 26, no. 1, pp. 298–306, Jan. 2011.

[33] A. Dekka, B. Wu, R. L. Fuentes, M. Perez, and N. R. Zargari, "Evolution of topologies, modeling, control schemes, and applications of modular multilevel converters," *IEEE J. Emerg. Sel. Topics Power Electron.*, vol. 5, no. 4, pp. 1631–1656, Dec. 2017.

[34] G. S. Konstantinou, M. Ciobotaru, and V. G. Agelidis, "Analysis of multi-carrier PWM methods for back-to-back HVDC systems based on modular multilevel converters," in *Proc. 37th Annu. Conf. IEEE Ind. Electron. Soc.*, 2011, pp. 4391–4396.

[35] G. S. Konstantinou and V. G. Agelidis, "Performance evaluation of half-bridge cascaded multilevel converters operated with multicarrier sinusoidal PWM techniques," in *Proc. 4th IEEE Conf. Ind. Electron. Appl.*, 2009, pp. 3399–3404.

[36] A. Hassanpoor, S. Norrga, H. Nee, and L. Ängquist, "Evaluation of different carrier-based PWM methods for modular multilevel converters for HVDC application," in *Proc. 38th Annu. Conf. IEEE Ind. Electron. Soc.*, 2012, pp. 388–393.

[37] M. Hagiwara and H. Akagi, "Control and experiment of pulsewidth-modulated modular multilevel converters," *IEEE Trans. Power Electron.*, vol. 24, no. 7, pp. 1737–1746, Jul. 2009.

[38] J. Pou, S. Ceballos, G. Konstantinou, V. G. Agelidis, R. Picas, and J. Zaragoza, "Circulating current injection methods based on instantaneous information for the modular multilevel converter," *IEEE Trans. Ind. Electron.*, vol. 62, no. 2, pp. 777–788, Feb. 2015.

[39] R. Darus, G. Konstantinou, J. Pou, S. Ceballos, and V. G. Agelidis, "Comparison of phase-shifted and level-shifted PWM in the modular multilevel converter," in *Proc. Int. Power Electron. Conf.*, 2014, pp. 3764–3770.

[40] B. Li, R. Yang, D. Xu, G. Wang, W. Wang, and D. Xu, "Analysis of the phase-shifted carrier modulation for modular multilevel converters," *IEEE Trans. Power Electron.*, vol. 30, no. 1, pp. 297–310, Jan. 2015.

[41] S. Lu, L. Yuan, K. Li, and Z. Zhao, "An improved phase-shifted carrier modulation scheme for a hybrid modular multilevel converter," *IEEE Trans. Power Electron.*, vol. 32, no. 1, pp. 81–97, Jan. 2017.

[42] C. D. Townsend, T. J. Summers, and R. E. Betz, "Impact of practical issues on the harmonic performance of phase-shifted modulation strategies for a cascaded H-bridge statcom," *IEEE Trans. Ind. Electron.*, vol. 61, no. 6, pp. 2655–2664, Jun. 2014.

[43] M. Huang, J. Zou, and X. Ma, "An improved phase-shifted carrier modulation for modular multilevel converter to suppress the influence of fluctuation of capacitor voltage," *IEEE Trans. Power Electron.*, vol. 31, no. 10, pp. 7404–7416, Oct. 2016.

[44] Y. Li, Y. Wang, and B. Q. Li, "Generalized theory of phase-shifted carrier PWM for cascaded H-bridge converters and modular multilevel converters," *IEEE J. Emerg. Sel. Top. Power Electron.*, vol. 4, no. 2, pp. 589–605, Jun. 2016.

[45] A. Allu, "Modelling and control of a grid-connected full bridge modular multilevel converter for integration of wind energy conversion systems," Ph.D. dissertation, Dept. Electron. Elect. Eng., Univ. Sheffield, Sheffield, U.K., 2019.

[46] A. Allu, M. Odavic, and K. Atallah, "Design considerations of a full bridge modular multilevel converter under variable DC link voltage," in *Proc. IEEE Energy Convers. Congr. Expo.*, 2017, pp. 504–510.

[47] K. Ilves, S. Norrga, L. Harnefors, and H. Nee, "On energy storage requirements in modular multilevel converters," *IEEE Trans. Power Electron.*, vol. 29, no. 1, pp. 77–88, Jan. 2014.

[48] D. G. Holmes and T. A. Lipo, *Pulse Width Modulation of Power Converters: Principles and Practice*. Piscataway, NJ, USA: Wiley, 2003.

[49] Q. Tu, Z. Xu, and L. Xu, "Reduced switching-frequency modulation and circulating current suppression for modular multilevel converters," *IEEE Trans. Power Deliv.*, vol. 26, no. 3, pp. 2009–2017, Jul. 2011.

[50] S. Thakur, M. Odavic, A. Allu, Z. Q. Zhu, and K. Atallah, "Theoretical harmonic spectra of PWM waveforms including DC bus voltage ripple — Application to low-capacitance modular multilevel converter," *IEEE Trans. Power Electron.*, vol. 35, no. 9, pp. 9291–9305, Sep. 2020.

[51] X. Li, Q. Song, W. Liu, S. Xu, Z. Zhu, and X. Li, "Performance analysis and optimization of circulating current control for modular multilevel converter," *IEEE Trans. Ind. Electron.*, vol. 63, no. 2, pp. 716–727, Feb. 2016.

Sumeet Singh Thakur was born in Hyderabad, India, on March 6, 1991. He received the B.Tech. degree in electrical engineering from the National Institute of Technology Warangal, Warangal, India, in 2012, and the M.Tech. degree in power electronics, electrical machines, and drives from the Department of electrical Engineering, Indian Institute of Technology, New Delhi, India, in 2016. He is currently working toward the Ph.D. degree in electrical engineering with the Department of Electronic and Electrical Engineering, University of Sheffield, Sheffield, U.K.

His research interests include design and control of power electronics converters and electrical machine drives.

Milijana Odavic (Member, IEEE) received the M.Sc. degree in electrical and electronic engineering from the University of Zagreb, Zagreb, Croatia, in 2004, and the Ph.D. degree in electrical engineering from the University of Nottingham, Nottingham, U.K., in 2008.

She is currently a Senior Lecturer in power electronics with the Department of Electronic and Electrical Engineering, University of Sheffield, Sheffield, U.K. Prior to joining the University of Sheffield, she was a Research Fellow with Power Electronics, Machines, and Control Group, University of Nottingham and with the Department of Electric Machines, Drives, and Automation, University of Zagreb. Her interests include of power electronics with particular focus on power conversion topologies, electronic power distribution systems, and modelling and control.

Ahmed Allu received the B.Sc. and M.Sc. degrees in electrical engineering from the University of Mosul, Mosul, Iraq, in 2002 and 2005, respectively, and the Ph.D. degree in electronic and electrical engineering from the University of Sheffield, Sheffield, U.K., in 2019.

He is currently an Assistant Professor with Electrical Techniques Department, Northern Technical University, Mosul, Iraq. His research interests include modelling and control of power electronic converters for emerging applications.

Z. Q. Zhu (Fellow, IEEE) received the B.Eng. and M.Sc. degrees from Zhejiang University, Hangzhou, China, in 1982 and 1984, respectively, and the Ph.D. degree from the University of Sheffield, Sheffield, U.K., in 1991, all in electrical and electronic engineering.

Since 1988, he has been with the University of Sheffield, where he currently holds the Royal Academy of Engineering/Siemens Research Chair and is the Head of the Electrical Machines and Drives Research Group, the Academic Director of Sheffield Siemens Wind Power Research Centre, the Director of CRRC Electric Drives Technology Research Centre, and the Director of Midea Electric Machines and Controls Research Centre. His current major research interests include the design and control of permanent-magnet brushless machines and drives for applications ranging from automotive through domestic appliances to renewable energy.

Dr. Zhu is a Fellow of the Royal Academy of Engineering.

Kais Atallah received the Ingenieur d'Etat degree in electrical engineering from Ecole Nationale Polytechnique, El-Harrach, Algeria, in 1988, and the Ph.D. degree from the University of Sheffield, Sheffield, U.K., in 1993.

He is currently a Professor of electrical engineering with the University of Sheffield. From 1993 to 2000, he was a Postdoctoral Research Associate with the Department of Electronic and Electrical Engineering, University of Sheffield. In 2006, he cofounded Magnomatics, Ltd., where he was the Director until July 2008. His research interests include fault-tolerant permanent magnet drives for safety-critical applications, magnetic gearing and "pseudo" direct drive electrical machines, and drive-trains for wind/tidal turbines and electrical/hybrid vehicles.